International Journal of Heat and Mass Transfer 133 (2019) 510–530

Contents lists available at ScienceDirect

International Journal of Heat and Mass Transfer

journal homepage: www.elsevier.com/locate/ijhmt

Enhanced model for annular flow in micro-channel heat sinks, including effects of droplet entrainment/deposition and core turbulence

Seunghyun Lee, Issam Mudawar *

Purdue University Boiling and Two-Phase Flow Laboratory (PU-BTPFL), School of Mechanical Engineering, Purdue University, 585 Purdue Mall, West Lafayette, IN 47907, USA

ARTICLE INFO

Article history:
Received 14 July 2018
Received in revised form 11 December 2018
Accepted 11 December 2018
Available online 28 December 2018

Keywords:
Micro-channels
Flow boiling
Annular flow
Eddy momentum diffusivity
Pressure drop
Heat transfer coefficient

ABSTRACT

This study investigates pressured drop and heat transfer characteristics for saturated flow boiling in a micro-channel heat sink specific to the annular flow regime. A theoretical control-volume-based model is presented, which relies on new relations for liquid droplet entrainment and deposition. While prior models have been attempted for annular flow, these models were based on simplified depictions of the vapor core based on average velocity. On the other hand, the present model provides detailed assessment of turbulence effects in the core, enabling the development of detailed cross-sectional profiles for momentum diffusivity, velocity, and shear stress. Predictive accuracy of the model is assessed against experimental data for R134a using a 609.6-mm long and 203.2-mm wide micro-channel heat sink containing 100 of 1 × 1-mm^2 flow channels. The model shows good accuracy against 69 experimental pressure drop data points, with mean absolute error (MAE) of 16.22%, and 97.10% and 100.0% of the data predicted within 30% and 50%, respectively. It also shows very good accuracy against 388 data points for local two-phase heat transfer coefficient, evidenced by a MAE of 8.35%, and with 98.45% and 99.74% of the data predicted within 30% and 50%, respectively.

1. Introduction

1.1. Implementation of two-phase mini/micro-channel cooling schemes

Recent efforts to cope with rising heat fluxes at device, module, and system levels in many modern applications have yielded an unprecedented number of published studies concerning both theory and implementation of two-phase cooling schemes [1–4]. During a period spanning over three decades, researchers at the Purdue University Boiling and Two-Phase Flow Laboratory (PU-BTPFL) have conducted extensive work concerning both fundamental mechanisms and applications of two-phase cooling schemes. They include investigations into pool boiling [5,6], falling film [7,8], macro-channel [9,10], micro-channel [11,12], jet impingement [13,14], and spray [15,16], as well as hybrid cooling schemes [17] combining the benefits of two or more of the aforementioned schemes.

A recent review article [18] showed how three of these two-phase cooling schemes have become the most serious contenders for very high flux applications: micro-channel, jet, and spray. While all three provide distinct advantages and drawbacks relative to one another, two-phase micro-channel cooling has received the most attention, especially during the past decade. This interest is the result of a number of intrinsic advantages of micro-channel heat sinks: compact, light-weight design, high cooling area to volume ratio, and small coolant inventory, let alone the ability to produce very high heat transfer coefficients [19]. Initial interest in implementing micro-channel cooling was focused on single-phase heat sinks [20–23]. But, despite their ability to achieve very high heat transfer coefficients, single-phase heat sinks suffer a fundamental drawback: large stream-wise increases in both fluid and device temperatures [19]. Two-phase micro-channel heat sinks can greatly reduce temperature gradients by relying on both latent and sensible heat (rather than sensible heat alone for the case of single-phase heat sinks), thereby maintaining temperatures close to the coolant's saturation temperature.

But two-phase micro-channel heat sinks are not without shortcomings. In 1994, Bowers and Mudawar [24] launched the first effort to predict both pressure drop and critical heat flux (CHF) for two-phase heat sinks, and provide a comprehensive assessment of practical concerns associated with implementing these devices in very high heat flux applications [25,26]. Key among those concerns is high pressure drop, which is accompanied by appreciable

---

* Corresponding author.
E-mail address: mudawar@ecn.purdue.edu (I. Mudawar).
URL: https://engineering.purdue.edu/BTPFL (I. Mudawar).

https://doi.org/10.1016/j.ijheatmasstransfer.2018.12.074
0017-9310/

Nomenclature

A	area
A^+	Kay's damping coefficient
A_{base}	total base area of heat sink
A_c	cross-sectional area of mixture core
A_{ch}	cross-sectional area of micro-channel
$A_{entrained}$	liquid flow area resulting from entrainment
$A_{f,*}$	flow area in liquid control volume
$A_{H,*}$	flow area in mixture core control volume
$A_{\delta_{exp}}$	experimental liquid flow area
a	damping coefficient in Eq. (64)
Bo	boiling number, $q''_H/G\,h_{fg}$
b	damping coefficient in Eq. (64)
C	liquid droplet concentration in mixture core
Ca	capillary number, $\mu_f G/(\rho_f \sigma)$
c_p	specific heat at constant pressure
D_h	hydraulic diameter
$D_{h,c}$	hydraulic diameter of mixture core
e	entrained droplet quality
F	function
F_{e0}	fraction of liquid entrained as droplets
f	fanning friction factor; liquid film quality
f_i	interfacial friction factor
G	mass velocity
H_{ch}	micro-channel height
H_{tc}	distance between thermocouple and bottom wall of micro-channel
h	enthalpy; heat transfer coefficient
h_{fg}	latent heat of vaporization
h_{tp}	two-phase heta transfer coefficient
K	Von-Karman constant, $K = 0.4$
k	deposition mass transfer coefficient; thermal conductivity
k_s	thermal conductivity of solid
L_{ch}	micro-channel length
l^+	dimensionless turbulent mixing length
$\dot{m}$	total mass flow rate of micro-channel module
N	number of Δz segments in finite difference scheme; number of data points
N_{ch}	number of micro-channels in heat sink
$P_{f,y}$	local perimeter at distance y from channel wall
$P_{f,\delta}$	interfacial parameter
P_H	heated perimeter of micro-channel
$P_{H,y}$	perimeter in homogeneous core mixture
P_R	reduced pressure, p/p_{crit}
Pr	Prandtl number
p	pressure
p_{crit}	critical pressure
Δp	pressure drop
Re	Reynolds number
Re_c	Reynolds number of mixture core
Re_{fo}	liquid only Reynolds number, GD_h/μ_f
Q	total heat input to heat sink
q''	heat flux at distance y from channel wall
q''_B	heat flux based on total base area of heat sink
q''_H	heat flux based on heated area of micro-channel
T	temperature
T^+	dimensionless temperature
T_w	micro-channel wall temperature
$T_{w,b}$	bottom wall temperature of micro-channel
u	velocity
u^+	dimensionless velocity
u^*	interfacial friction velocity
u^*_w	wall friction velocity
u_i	interfacial velocity
$\bar{u}_c$	mean velocity of vapor core
$\bar{u}_f$	mean liquid film velocity
v	specific volume
v_{fg}	specific volume difference between vapor and liquid
W	deposition rate
W_{ch}	micro-channel width
We_{fo}	liquid-only Weber number, $G^2 D_h/(\rho_f \sigma)$
W_w	half-width of copper sidewall separating micro-channels
x	vapor quality
x_0	vapor quality at onset of annular flow
x_c	effective mixture core quality
x_e	thermodynamic equilibrium quality
y	perpendicular distance from micro-channel wall
y^+	dimensionless distance perpendicular to micro-channel wall, $y^+ = yu^*/\nu_f$
z	axial coordinate

Greek symbols

α	void fraction; iteration coefficient
β	channel aspect ratio
β_c	aspect ratio of mixture core
Γ_d	droplet deposition rate per unit channel length
Γ_{fg}	evaporation rate per unit channel length
δ	thickness of annular liquid film
δ^+_H	dimensionless mixture core thickness, yu^*/ν_H $(\delta \le y \le H_{ch}/2)$
$\delta_{e=0}$	calculated liquid film thickness without droplet entrainment
ε_m	eddy momentum diffusivity
η	fin efficiency
θ	percentage predicted within ±30%
μ	dynamic viscosity
ν	kinematic viscosity
ξ	percentage predicted within ±50%
ρ	density
ρ_H	homogeneous core mixture density
σ	surface tension
τ	shear stress
ϕ^2_f	frictional pressure drop multiplier
ω	coefficient in Beattie and Whalley viscosity model

Subscripts

0	location of onset of annular flow
A	accelerational
ann	annular flow
c	contraction; mixture core
cor	correlation
e	entrained liquid droplets
exp	experimental (measured)
F	frictional
f	saturated liquid; liquid film
fo	liquid-only
g	saturated vapor
H	homogeneous mixture
i	liquid-vapor interface
in	micro-channel inlet
max	maximum
mb	momentum balance
opt	optimum
out	micro-channel outlet
pred	predicted
sat	saturation

sp	single-phase liquid
tc	thermocouple
tp	two-phase
w	micro-channel wall
Wallis	based on Wallis treatment
z	local property along axial direction

compressibility and flashing, as well as increased likelihood for two-phase choking. Bowers and Mudawar pointed out these concerns may be alleviated by relying on accurate predictive tools for both pressure drop and heat transfer.

1.2. Thermal management for space missions using large length-to-diameter micro-channel heat sinks

Future long-term manned space missions, especially to Mars, are projected to greatly increase the space vehicle's power input and heat rejection. The vehicle's Thermal Control System (TCS) plays the primary role in tackling heat rejection from both astronauts and avionics, as well as maintaining acceptable temperature and humidity. Key to successful design of the vehicle is reducing weight and volume of all internal sub-systems, including the TCS and all its subcomponents [27–29].

The TCS has three primary heat management duties: acquisition, transport, and rejection. Using a closed coolant flow loop, both metabolic heat and heat produced by the avionics are extracted using a variety of heat exchange equipment, and transferred to yet another heat exchanger from which the heat is rejected by radiation to deep space. All earlier TCS architectures, includes those used onboard NASA's space shuttles, involved use of single-phase cooling loops, which are now deemed far too heavy for future space missions. This is why focus has recently shifted to cooling loops that rely on evaporation and condensation of an appropriate coolant to, respectively, extract and reject the heat. The primary benefit in using a two-phase cooling loop is ability to achieve orders of magnitude enhancement in both evaporation (by boiling) and condensation heat transfer coefficients, thereby greatly reducing both weight and volume of heat exchange components for a given total heat load.

Since the early 2000s, researchers at PU-BTPFL have performed extensive work related to adaptation of two-phase TCS technologies, including mechanisms, assessment of prior predictive tools, and development of new predictive models; these studies involved both ground and parabolic flight microgravity experiments [30–33]. More recently, efforts were focused on thermodynamic considerations [34], with emphasis on specific space vehicles, including Orion. They showed anticipated heat loads could be effectively removed with the aid of a two-phase loop utilizing micro-channel evaporators having multiple parallel channels with large length-to-diameter ratio [35–37].

Several important issues must be addressed when employing a micro-channel evaporator to dissipate the heat in a TCS cooling loop. First, coolant mass velocity within the micro-channels must be kept high enough to both achieve high heat transfer coefficients [38–41] and avoid dry-out [35–37]. For a fixed total flow rate, mass velocity may be increased by having fewer parallel evaporator channels. On the other hand, relying on fewer channels increases pressure drop and associated aforementioned problems, including excessive compressibility and flashing, and increased likelihood of two-phase choking [42,43]. Another practical concern is achieving equal distribution of coolant flow among the parallel channels, which requires careful design of inlet and exit plenums. Proper sizing of the plenums also helps maintain constant inlet and outlet pressures, and guards against certain types of flow instabilities.

1.3. Prior predictive methods for pressure drop and heat transfer coefficient in two-phase micro-channel flows

By far the vast majority of available methods for predicting two-phase pressure drop in channels are based on either the Homogeneous Equilibrium Model (HEM) [44–49] or empirical/semi-empirical formulations [50–55]. The semi-empirical tools, many of which being based on the Lockhart-Martinelli [55] separated flow formulation, have been especially popular in recent years. However, correlations are often based on databases for few fluids and limited ranges of operating and geometrical parameters, and extrapolating these correlations beyond the validity range for which they were originally intended has been shown to yield unusually large predictive errors.

A powerful alternative is use of 'universal correlations,' which rely on massive databases from many sources, and which cover numerous fluids and very broad ranges of operating and geometrical parameters. In recent years, universal correlations have shown great success in predicting several important micro-channel parameters, including pressure drop [38], heat transfer coefficient, and dryout [39–41], and choking [42].

Given the tendency for flow boiling in micro-channels to produce annular flow over a large fraction of the channel length, another powerful technique to predict both pressure drop and heat transfer coefficient is the analytical control volume method, where mass, momentum, and energy conservation laws are applied to control volumes encompassing the vapor core and liquid film separately, with appropriate velocity, shear stress, temperature, and heat flux applied along the vapor-liquid interface. This method has shown great versatility and success in predicting thermal behavior in pool boiling [56], flow boiling [9], and falling films [57]. The accuracy of these models is highly dependent on appropriate use of eddy diffusivity relations to account for turbulent effects within each phase and interfacial damping of turbulence along the liquid-vapor interface.

1.4. Objectives of study

The present study is part of a series of joint investigations between the Purdue University Boiling and Two-Phase Flow Laboratory (PU-BTPFL) and the NASA Glenn Research Center (GRC), whose ultimate goal is to develop two-phase thermal management design tools for future space vehicles.

In this study, the control volume method is used to develop analytical models for pressure drop and heat transfer coefficient in two-phase micro-channel heat sinks. Unlike prior attempts at predicting the same performance parameters using the control volume method [58–60], which employed average velocity calculations for the vapor core, the present study involves detailed prediction of velocity profiles across both the vapor core and annular liquid film. Accuracy of the models is examined in detail by comparing predictions to data for both pressure drop and heat transfer coefficient.

2. Experimental methods

2.1. Two-phase flow loop

Fig. 1(a) shows a schematic of the flow loop that is configured to deliver subcooled R134a to a test module containing parallel micro-channels sharing inlet and outlet plenums. The test module serves as evaporator for the loop, wherein electrical energy is supplied to the fluid, changing the fluid state from subcooled liquid to saturated two-phase mixture.

The two-phase mixture exiting the test module is routed through an air-cooled condenser, which removes heat from the fluid and returns the fluid to subcooled liquid state. A solid-state controller is used to regulate the condenser's fan speed in response to the condenser's downstream temperature. A tee-junction downstream from the condenser leads to a 10-gallon liquid reservoir

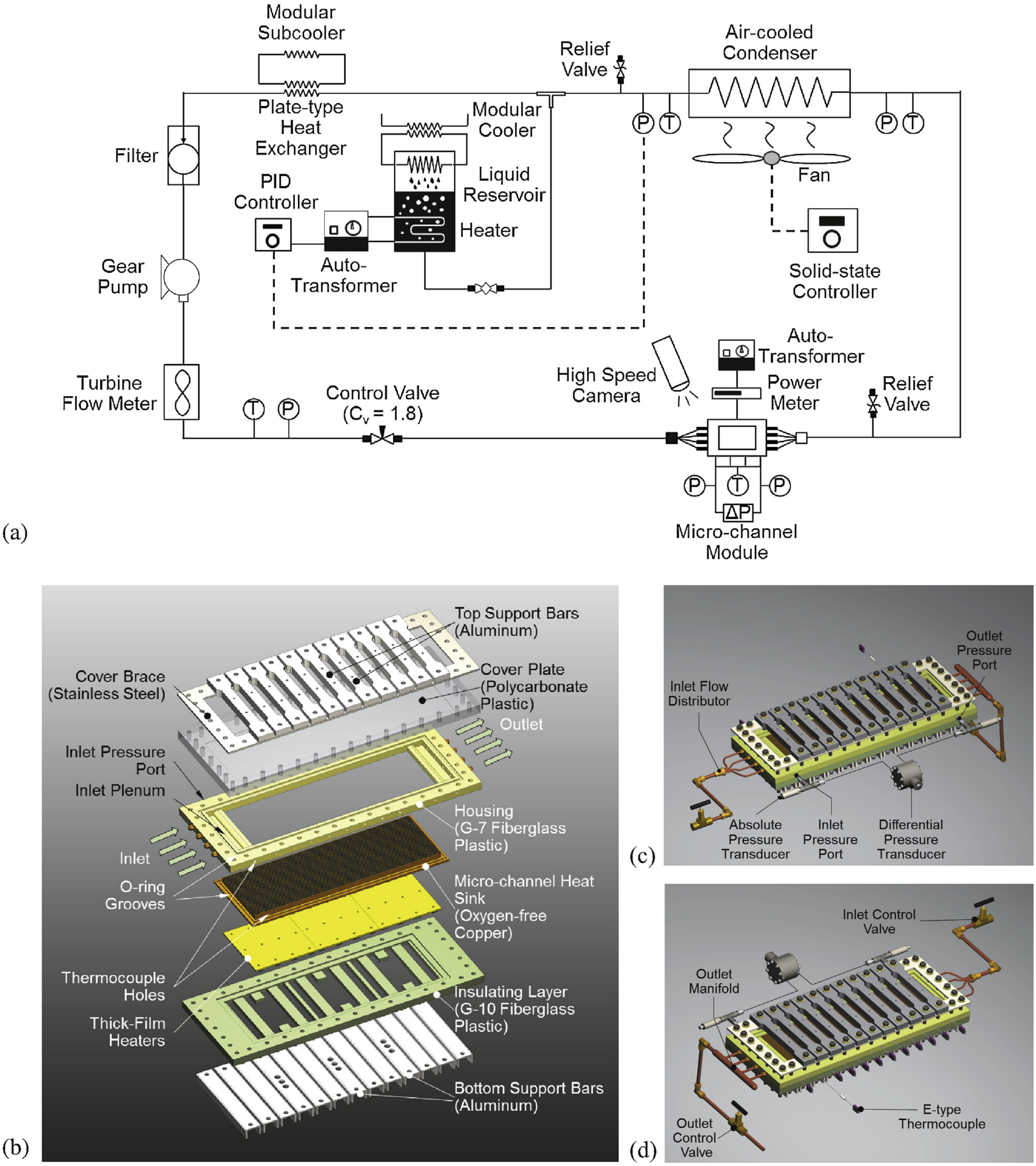

Fig. 1. (a) Schematic diagram of two-phase loop. (b) 3D CAD stacked rendering of micro-channel module. Assembled module with (c) pressure and (d) temperature measurement instrumentation.

containing electrical immersion heaters. A PID controller is used to regulate power input to the immersion heaters, providing precise production of vapor inside the reservoir in response to the difference between condenser outlet pressure and PID set-pressure. And, mounted in the top portion of the reservoir is a condensing coil, which rejects heat from the fluid to an external modular water-cooling system. Combination of vapor production and condensation in the reservoir, along with the PID control, provides a stable reference pressure set point at the tee-junction.

Further subcooling is achieved by passing the fluid through a plate-type heat exchanger situated downstream of the tee-junction. This heat exchanger rejects heat from the fluid to a second modular water-cooling system, ensuring that the R134a is fully converted to liquid state. Exiting this heat exchanger, the subcooled fluid is routed to a gear pump followed by a turbine flow meter. A throttling valve, situated between the turbine flow meter and test module, is used to both regulate flow rate and help combat pressure-drop oscillations within the test module.

2.2. Micro-channel test module construction and instrumentation

The micro-channel test module is comprised of a stack of multiple layers as shown in Fig. 1(b). The main layer is a copper heat sink, having 100 of 1 × 1-mm^2 square flow channels. The heat is supplied from thick-film resistors fitted to the underside of the copper heat sink. The heat is conducted through the copper heat sink and supplied to the fluid passing through the channels. The heat sink is surrounded along its perimeter and below the thick-film resistors by insulating layers made from G-7 and G-10 fiberglass plastic, respectively. The G-7 layer also provides inlet and outlet plenums for the micro-channels. The tops of the micro-channels are sealed off with the aid of a transparent polycarbonate cover plate, which also provides optical access to the flow along the micro-channels. The test module also includes a top stainless steel brace and top/bottom aluminum support bars, which serve to prevent fluid leaks from the micro-channels as well as enhance structural integrity of the entire test module assembly.

As shown in Fig. 1(c), steady-state pressure drop across the micro-channels is measured with the aid of two Omega-MMA absolute pressure transducers, one installed in the test module's inlet plenum and another in the outlet plenum. Additionally, any fluctuations in pressure drop across the micro-channels are measured with a Honeywell-THE differential pressure transducer connected between the inlet and outlet plenums.

Axial variations of the copper heat sink temperature are measured by a series of 10 type-E thermocouples inserted laterally across, Fig. 1(d), with their tips reaching the centerline of the heat sink. Axial locations of these thermocouples are provided in Table 1. Precise temperature measurements are the result of high Seebeck coefficient, 66 μV/°C, of type-E thermocouples, along with careful calibration of each thermocouple over a range of −22.5 to 80 °C [35–37]. Additional type-E thermocouples are inserted into the flow at various locations along the flow loop external to the test module itself.

Power input to the thick film heaters and volumetric flow rate are measured by a Yokogawa W230 power meter and an FTO Flow Technology flow meter, respectively. Signals from the pressure transducers, thermocouples, power meter, and turbine flow meter are collected using a Data FET multiplexer and voltmeter, and processed using LabView software. Axial changes in interfacial behavior along the channels was captured with the aid of an Ultima APX high speed camera fitted with Micro Nikkor 105-mm lens at a shutter speed 1/8000 s, using a fiber optic light source.

Table 1
Micro-channel heat sink dimensions.

Length [mm]	Width [mm]	Number of channels	Axial locations of thermocouples [mm]
609.6	203.2	100	44.2, 102.1, 160.0, 217.9, 275.8, 333.8, 391.7, 434.3, 507.5, 565.4

Measurement uncertainties are estimated at ±0.1%, ±0.1%, ±0.1 °C, ±0.12%, and ±0.3% for absolute pressure, differential pressure, temperature, mass flow rate, and heat input, respectively. Using the root-sum-square method [61,62], maximum uncertainties propagated in calculating heat transfer coefficient, pressure drop, and vapor quality increment are estimated at 13.46%, 0.1%, 0.16%, respectively.

Fig. 2(a) provides additional details of the test module assembly and heat sink construction. Notice that the top micro-finned surface of the heat sink measures 609.6-mm long and 203.2-mm wide, providing a micro-channel length-to-diameter ratio of 609.6. This ratio is vitally important to the findings from the present study, by providing a broad axial span to capture large variations in both two-phase flow pattern and heat transfer coefficient, compared to much shorter micro-channel modules employed in prior studies. This high ratio also provides better representation of 'cold plates' used for cooling of electronic and avionic hardware.

2.3. Operating conditions and determination of heat transfer coefficient

Coolant is supplied to the test module in subcooled liquid state and changes to saturated mixture as it absorbs heat moving along the channels. The phase change is estimated to occur at the axial location where the coolant reaches saturation temperature, T_{sat}, and thermodynamic equilibrium quality, x_e, is equal to zero. Quality at the test module's inlet, $x_{e,in}$, is determined from the relation

$$x_{e,in} = \frac{h_{in} - h_f}{h_{fg}} = -\frac{c_{p,f}(T_{sat} - T_{in})}{h_{fg}}, \tag{1}$$

where $c_{p,f}$ and h_{fg} are the coolant's specific heat and latent heat, respectively, based on the the measured inlet pressure, and T_{in} is the measured inlet temperature. The outlet quality is determined by applying energy balance to the entire module,

$$x_{e,out} = x_{e,in} + \left(q''_B A_{base}\right)/\dot{m} h_{fg}, \tag{2}$$

where q''_B is heat flux based on the 609.6-mm long by 203.2-mm wide area, A_{base}, of the heat sink, and $\dot{m}$ the total flow rate of R134a. Table 2 provides ranges of key parameters of the present study, including, aside from $x_{e,in}$, $x_{e,out}$, and q''_B, inlet pressure, p_{in}, and mass velocity, G.

Fig. 2(b) provides a detailed cross-sectional representation of a unit cell used in development of the present model. It consists of single channel and two half-width sidewalls, and shows heat flux from the thick film resistor supplied to the heat sink's underside, conducted across the heat sink and into the channel bottom wall and sidewalls, before being convected to the coolant. The two-phase heat transfer coefficient, h_{tp}, is determined by treating the sidewalls as adiabatic tip fins with efficiency of η,

$$h_{tp} = \frac{q''_B(W_{ch} + 2W_w)}{\left(T_{w,b} - T_{sat}\right)\left(W_{ch} + 2\eta H_{ch}\right)} \tag{3}$$

where W_{ch} (=1 mm), W_w (=0.5 mm), and H_{ch} (=1 mm) are the micro-channel width, sidewall half-width, and channel height, respectively. Temperature $T_{w,b}$ in Eq. (3) corresponds to the micro-channel's bottom wall, and is determined from the thermocouple measured temperature, T_{tc}, by assuming one-dimensional conduction between the T_{tc} and $T_{w,b}$ planes, $T_{w,b} = T_{tc} - q''_B H_{tc}/k_s$, where H_{tc} and k_s are distance between thermocouple junction and

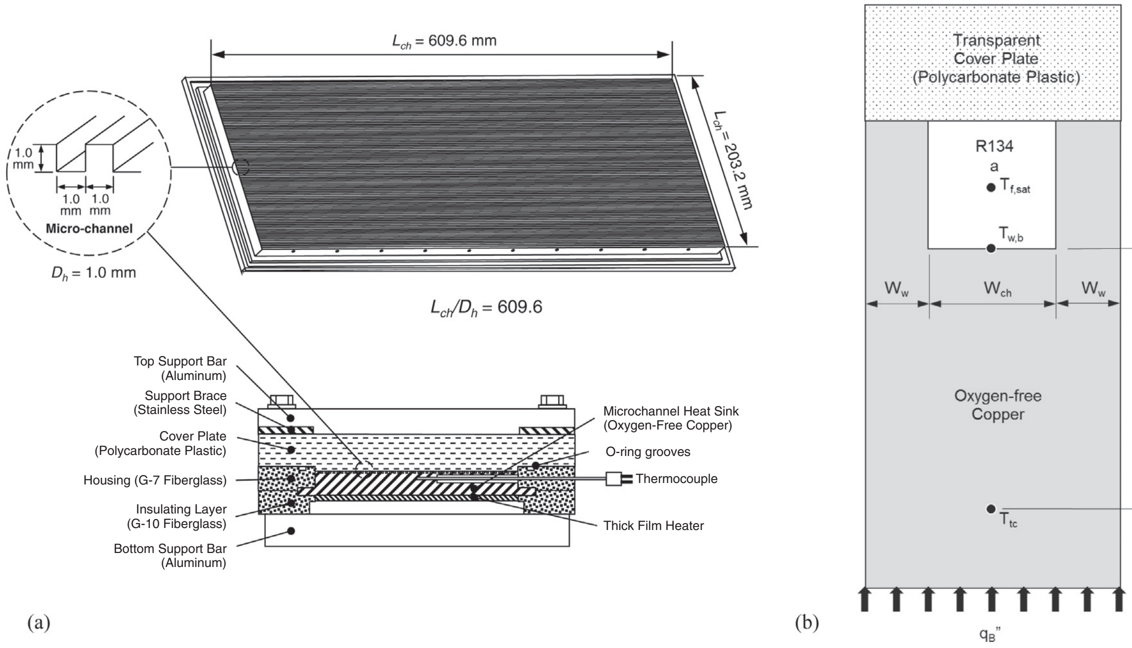

Fig. 2. (a) Cross-sectional view of micro-channel module and details of the copper heat sink design. (b) Two-dimensional micro- channel unit cell.

Table 2
Operating conditions of micro-channel heat sink module.

G [kg/m^{2}s]	q_B"[W/m^2]	$x_{e,in}$	$x_{e,out}$	p_{in}[kPa]
75.92–208.79	3990–28,209	−0.041 to −0.022	0.096–0.956	688.3–731.3

channel's bottom wall, and thermal conductivity of copper, respectively. In Eq. (3), T_{sat} is determined by interpolating between inlet and outlet plenum saturation temperatures, both based on corresponding measured plenum pressures.

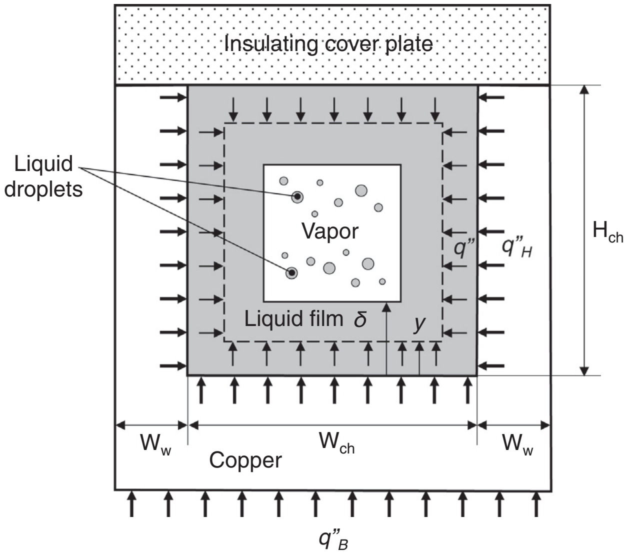

Fig. 3. Schematic of channel cross-section used in annular flow model.

3. Annular flow model development

3.1. Model assumptions

The annular flow model presented here employs some of the same basic assumptions employed in two previous studies [59,60] but features crucial differences in terms of ability to predict detailed velocity and temperature profiles, something not available in the earlier studies. Fig. 3 shows a cross-sectional schematic of a single unit cell, and identifies key parameters used in the model. The flow consists of an annular liquid film of thickness δ covering all four inner walls of the channel, surrounding a vapor core, which also contains liquid droplets that are formed by interfacial breakup of the liquid film. The droplets are formed by upstream shattering upon initiation of the annular flow regime and gradually deposited along the channel. Notice that the heat is transferred to the liquid film along three walls, bottom wall and two sidewalls, while the top wall is insulated. Being different from a uniformly heated circular channel, three different heat fluxes are defined and used in the model: heat flux along the base area of the heat sink, q''_B, average heat flux along the channel's bottom wall and sidewalls, q''_H, and local heat flux in the liquid film, q'', at distance y from the channel walls, were

$$q''_B = \frac{\dot{m}(h_{out} - h_{in})}{(W_{ch} + 2W_w)L_{ch}}, \tag{4}$$

$$q''_H = \frac{q''_B(W_{ch} + 2W_w)}{(W_{ch} + 2H_{ch})}, \tag{5}$$

and

$$q'' = \frac{q''_H(W_{ch} + 2H_{ch})}{(W_{ch} - 2y)(H_{ch} - 2y)}. \tag{6}$$

Following are key assumptions employed in the model:

1. The annular flow is steady and concurrent.
2. Pressure is uniform across the channel's cross-section.
3. Thermodynamic equilibrium is maintained along the channel.
4. Gravitational effects are negligible.

5. The liquid film interface is smooth, and its thickness uniform along all four inner channel walls.
6. Axial momentum changes in the liquid film are negligible due to small liquid velocity gradient compared to that of the core mixture.
7. Mass transfer by evaporation and droplet deposition occurs only along the film interface.
8. Heat flux is uniform at any distance y across the film, as well as along the interface.
9. Liquid droplets are entrained into the core by shattering of liquid ridges from upstream slug flow at the onset of annular flow, and no further liquid entrainment occurs downstream.
10. Entrained droplets are uniformly distributed within the core.
11. Entrained liquid droplets are deposited upon the interface gradually in the flow direction.
12. Vapor and entrained droplets of the mixture core maintain equal velocities and are at same saturation temperature; *i.e.*, no temperature gradients are considered across the mixture core.
13. Eddy momentum diffusivity at the liquid film interface is zero because of turbulence suppression resulting from surface tension [60,63].

3.2. Model formulation

3.2.1. Control volume analysis

3.2.1.1. Mass conservation. Total mass flow rate, $\dot{m}$, is the sum of flow rates of the liquid film, $\dot{m}_f$, entrained droplets, $\dot{m}_e$, and vapor, $\dot{m}_g$,

$$\dot{m} = \dot{m}_f + \dot{m}_e + \dot{m}_g. \tag{7}$$

Individual qualities for the three components of the flow are calculated as ratios of individual mass flow rates to total flow rate. Therefore, three different qualities are used: liquid film quality, f, entrained liquid droplet quality, e, and vapor quality, x, where

$$f = \frac{\dot{m}_f}{\dot{m}}, \tag{8}$$

$$e = \frac{\dot{m}_e}{\dot{m}}, \tag{9}$$

and

$$x = \frac{\dot{m}_g}{\dot{m}}. \tag{10}$$

From assumption (3), vapor quality in the saturated region ($0 \leqslant x_e \leqslant 1$) is set equal to thermodynamic equilibrium quality, x_e,

$$x = x_e = \frac{h - h_f}{h_{fg}}. \tag{11}$$

Mass conservation is applied to the unit control volume depicted in Fig. 3 to determine variations of mass flow rates of the liquid film, entrained droplets, and vapor in direction z along the channel.

$$\frac{d\dot{m}_f}{dz} = \Gamma_d - \Gamma_{fg}, \tag{12}$$

$$\frac{d\dot{m}_e}{dz} = -\Gamma_d, \tag{13}$$

and

$$\frac{d\dot{m}_g}{dz} = \Gamma_{fg}, \tag{14}$$

where Γ_d and Γ_{fg} are the droplet deposition rate per unit length and evaporation rate per unit length, respectively.

Mass flow rate of the liquid film is calculated by integrating the film's velocity profile,

$$\dot{m}_f = \rho_f \int_0^{\delta} u_f(y) P_{f,y} dy, \tag{15}$$

where u_f and $P_{f,y}$ are, respectively, the local liquid velocity and perimeter at distance y from the channel walls. And the rates of mass transfer due to evaporation and droplet deposition are expressed as

$$\Gamma_{fg} = \frac{q''_H P_H}{h_{fg}}, \tag{16}$$

and

$$\Gamma_d = W\, P_{f,\delta}. \tag{17}$$

where P_H, $P_{f,\delta}$ and W are the 3-sided (channel bottom wall and two sidewalls) heated perimeter, interfacial perimeter, and droplet deposition rate, respectively, and heat flux q''_H is determined by dividing total electrical power input, Q, by heated area of channels (*i.e.*, excluding top insulated area), $q''_H = Q/(N_{ch} P_H L_{ch})$. Given the assumption that liquid droplets in the mixture core are assumed uniformly distributed in the core, and to avoid incorporating all complexities of the deposition process [64–67], the deposition rate, is assumed to depend solely on liquid droplet concentration rate, $W = k\, C$, where k is the deposition mass transfer coefficient, and $C = \dot{m}_e/(\dot{m}_e v_f + \dot{m}_g v_g)$. Previous investigators [59,60,64,66] employed empirical correlations to determine coefficient k using a formulation by Paleev and Filippovich [68] (some aided by flow regime maps [69]) in which local quality, e, of entrained droplets is determined from 'experimental film thickness', δ_{exp}, obtained from the measured heat transfer coefficient, h_{exp}, according to the relation

$$h_{\exp} = \frac{k_f}{\int_0^{\delta_{\exp}} \frac{(W_{ch}+2H_{ch})}{2(W_{ch}-2y)+2(H_{ch}-2y)} dy}. \tag{18}$$

Initial numerical results using the present annular flow model sans consideration of liquid droplet entrainment showed that velocity profile across the liquid film increases linearly from zero at the wall to velocity u_i at the liquid-vapor interface. The linear approximation is deemed quite reasonable given the small film thickness rendering the film flow both laminar and driven entirely by interfacial shear. With this linear profile, average velocity of the liquid film, $\bar{u}_f$, is one half that of the interface, $\bar{u}_f = 1/2 u_i$. Assuming the liquid droplets are entrained into the mixture core at the interfacial velocity, u_i, the average film velocity is calculated according to

$$\bar{u}_f = \frac{(1 - x_e) G A_{ch}}{\rho_f (A_{\delta_{\exp}} + 2A_{entrained})}, \tag{19}$$

where $A_{\delta_{\exp}}$ and $A_{entrained}$ are the liquid film flow area and liquid flow area resulting from the entrainment, both based on δ_{exp}.

$$A_{\delta_{\exp}} = W_{ch} H_{ch} - (W_{ch} - 2\delta_{\exp})(H_{ch} - 2\delta_{\exp}) \tag{20}$$

and

$$A_{entrained} = (W_{ch} - 2\delta_{\exp})(H_{ch} - 2\delta_{\exp}) - (W_{ch} - 2\delta_{e=0})(H_{ch} - 2\delta_{e=0}), \tag{21}$$

where $\delta_{e=0}$ is the liquid film thickness calculated without the liquid droplet entrainment. The local quality of entrained liquid droplets at any axial location z based on δ_{exp} is expressed as

$$e_{z,\exp} = \frac{\dot{m}_{e,z}}{\dot{m}} = \frac{2(1 - x_e) A_{entrained}}{(A_{\delta_{\exp}} + 2A_{entrained})}, \tag{22}$$

which is used for calculating local value for coefficient k along the channel [70],

$$k = -GA_{ch}\left(\frac{e_{z,\exp}-e_0}{z_{\exp}-z_0}\right)\left(\frac{1}{P_{\delta,\exp}C}\right), \tag{23}$$

which can be expressed as

$$\Gamma_d = -GA_{ch}\frac{e_{z,\exp}-e_0}{z_{\exp}-z_0}. \tag{24}$$

where e_0, $e_{z,\exp}$, z_0, and z_{exp} are initial entrainment quality, local liquid droplet quality, distance from inlet to onset of annular flow, and distance from inlet to local entrainment position, respectively. Whalley [65] recommended relation $e_0 = 0.99F_{e0} = 0.99(1-x_0)$ for initial approximation of e_0 to calculate k, but the value for e_0 in the present study is determined by empirical correlation fitted against experimental results.

The new relation for k is developed by correlating experimental data from the present study using least-squares' method relative to boiling number, Bo, as shown in Fig. 4,

$$\frac{k}{\bar{u}_c} = 1.916Bo\left(\frac{C}{\rho_H}\right)^{-0.563}, \tag{25}$$

where $\bar{u}_c$, ρ_H, and x_c are mean core velocity, core homogeneous mixture density, and effective quality of vapor in the core, which are defined, respectively, as

$$\bar{u}_c = \frac{\dot{m}_e + \dot{m}_g}{\rho_H A_c}, \tag{26}$$

$$\rho_H = \frac{1}{x_c v_g + (1-x_c)v_f}, \tag{27}$$

and

$$x_c = \frac{\dot{m}_g}{\dot{m}_g + \dot{m}_e}, \tag{28}$$

and A_c is cross-sectional area of the core, $A_c = (W_{ch}-2\delta)(H_{ch}-2\delta)$.

Qu and Mudawar [59] and Kim and Mudawar [60] used Taitel and Dukler's [69] adiabatic flow regime map for horizontal macro-channels to determine the quality corresponding to onset of annular flow, x_0, in mini/micro-channels. They assumed the onset of annular flow is determined by the boundary between bubbly and annular flow regimes, and used the Lockhart-Martinelli [55] parameter to predict this quality. However, the present model employs the boundary between slug and transition flow regimes as onset of annular flow, based on a recent flow regime map developed by the present authors for flow boiling in square micro-channel heat sinks [37],

$$x_0 = \left[1 + \left(\frac{\mu_g}{\mu_f}\right)^{1/9}\left(\frac{v_g}{v_f}\right)^{5/9}\right]^{-1}. \tag{29}$$

The above equation predicts x_0 values from 0.157 to 0.162, which are slightly higher than those based on macro-channel maps, 0.151–0.156 [59] and 0.144–0.148 [60]. Fig. 5 shows a schematic of initial droplet entrainment resulting from liquid shattering in the channel, along with a series of high speed video images captured at the moment of shattering at $z = 333.76$ mm for $G = 94.9$ kg/m^{2}s and $q''_B = 12{,}109$ W/m^2. The entrained droplets are shown traveling along the mixture core at relatively high speed. As indicated in Table 2, the present study is focused entirely on subcooled inlet conditions. Therefore, the present model addresses only the annular region, and data for the upstream flow regimes are excluded from analysis.

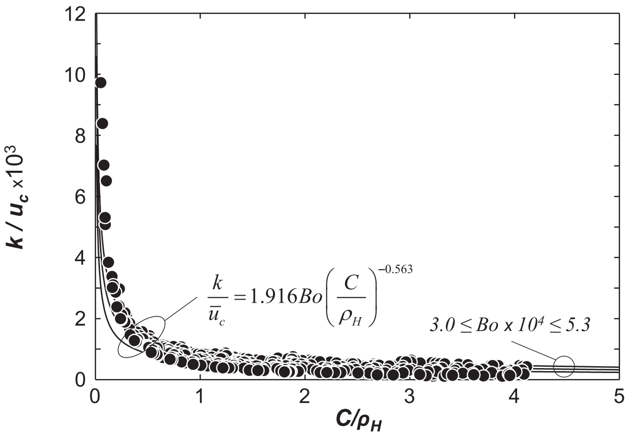

Fig. 4. Variation of dimensionless deposition mass transfer coefficient with dimensionless droplet concentration in the core.

For initial entrained liquid droplet quality, e_0, Whalley et al. [65] suggested the relation $e_0 = 0.99F_{e,0}$, where $F_{e,0} = \dot{m}_{e,0}/(\dot{m}_{f,0} + \dot{m}_{e,0})$, based on a rather arbitrary initial annular flow vapor quality of $x_0 = 0.01$. While this approach and initial vapor quality value provided reasonable predictions of experimental data by Qu and Mudawar [59] for flow boiling in rectangular micro-channel heat sinks, Qu and Mudawar opted for their own correlation for initial entrained droplet quality, which was based on liquid-only Weber number, $We_{fo} = G^2 D_h v_f/\sigma$, while Kim and Mudawar [60] correlated initial entrained droplet quality to both Capillary number, $Ca = \mu_f G/\rho_f\sigma = We_{fo}/\mathrm{Re}_{fo}$, and reduced pressure, $P_R = p/p_{crit}$.

In the present study, a new correlation is proposed for initial entrained liquid droplet quality, which is based on ability to predict the present heat transfer coefficient data with the lowest mean absolute error (MAE). This quality is correlated iteratively with respect to boiling number, Bo, based on 69 experimental data sets,

$$e_0 = 0.785 + 199.34Bo^{1.123}, \tag{30}$$

as shown in Fig. 6.

3.2.1.2. Momentum conservation. Momentum conservation is applied to two different control volumes of axial length Δz, the first extending from within the annular liquid film to the interface, Fig. 7(a), and the second from within the core to the interface, Fig. 7(b). Fig. 7(a) depicts momentum and force components associated with the former control volume. This control volume is bound by perimeter $P_{f,y}$, measured within the liquid film at distance y perpendicular to the channel wall, and inner perimeter, $P_{f,\delta}$, corresponding to the interface. Momentum interactions and force components acting on the liquid control volume are balanced according to following equation, assuming deposition and evaporation take place at mixture core mean velocity, $\bar{u}_c$, and interfacial velocity, u_i, respectively,

$$\Gamma_{fg}u_i\Delta z - \Gamma_d\bar{u}_c\Delta z = pA_{f,*} - \left(p + \frac{dp}{dz}\Delta z\right)A_{f,*} - \tau_f P_{f,y}\Delta z + \tau_i P_{f,\delta}\Delta z, \tag{31}$$

where $A_{f,*}$ is flow area of the liquid control volume, which is defined in Table 3. The liquid film's acceleration, $\partial/\partial z\left(\int_y^\delta \rho_f u_f^2 P_{f,y}dy\right)$, and pressure force associated with axial changes in flow area, $p(dA_{f,*}/dz)\Delta z$, are ignored because of their comparatively small magnitude. Rearranging Eq. (31) yields the following relation for shear stress across the liquid film,

$$\tau_f = \frac{1}{P_{f,y}}\left[\left(-\frac{dp}{dz}\right)A_{f,*} + \left(\tau_i P_{f,\delta} + \Gamma_d\bar{u}_c - \Gamma_{fg}u_i\right)\right]. \tag{32}$$

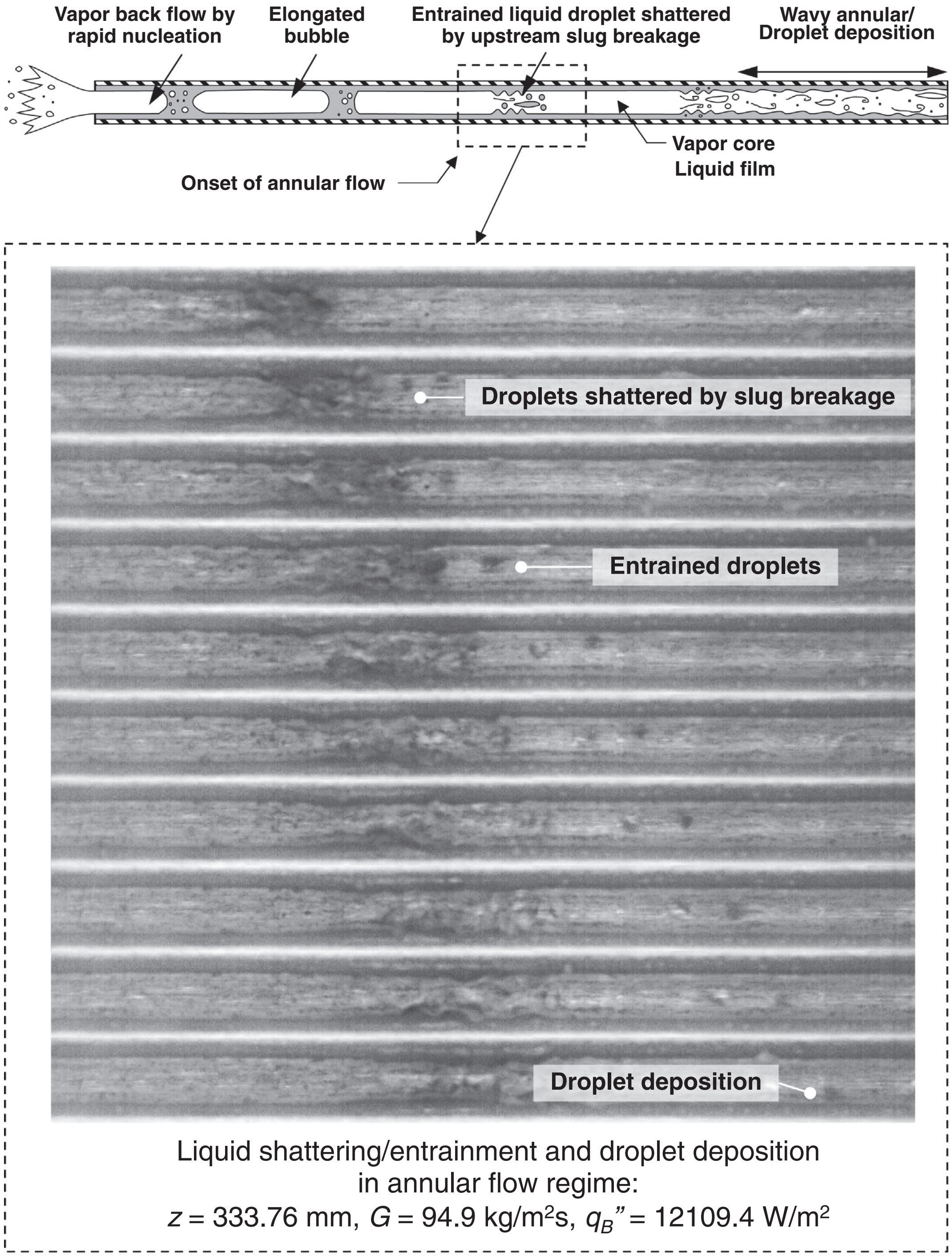

Fig. 5. Schematic of flow regime changes along the channel and droplet entrainment by liquid shattering in middle of channel, and series of high speed video images showing liquid slug breakup and droplet entrainment corresponding to transition from slug to annular flow. The time interval between consecutive images is 0.625 ms.

It is assumed the liquid film flow is laminar (common to most micro-channel flows), and the shear stress is related to velocity gradient within the film according to

$$\tau_f = \mu_f \frac{du_f}{dy}. \tag{33}$$

Equating Eqs. (32) and (33) provides the following relation for liquid film velocity profile,

$$u_f(y) = \frac{\delta}{\mu_f}\left(-\frac{dp}{dz}\right)\int_0^{y/\delta}\frac{A_{f,*}}{P_{f,y}}d\left(\frac{y}{\delta}\right) + \frac{\delta}{\mu_f}\left(\tau_i P_{f,\delta} + \Gamma_d \bar{u}_c - \Gamma_{fg} u_i\right)\int_0^{y/\delta}\frac{1}{P_{f,y}}\left(\frac{y}{\delta}\right), \tag{34}$$

which, by setting $y = \delta$, can be used to derive a relation for interfacial velocity,

$$u_i = \frac{\left(-\frac{dp}{dz}\right)\int_0^1 \frac{A_{f,*}}{P_{f,y}} d\left(\frac{y}{\delta}\right) + \left(\tau_i P_{f,\delta} + \Gamma_d \bar{u}_c\right)\int_0^1 \frac{1}{P_{f,y}} d\left(\frac{y}{\delta}\right)}{\frac{\mu_f}{\delta} + \Gamma_{fg}\int_0^1 \frac{1}{P_{f,y}} d\left(\frac{y}{\delta}\right)}. \tag{35}$$

Eq. (34) can be coupled with mass conservation, Eq. (15), to yield an expression for the pressure gradient,

$$-\frac{dp}{dz} = \frac{\frac{\mu_f \dot{m}_f}{\rho_f \delta^2} - \left(\tau_i P_{f,\delta} + \Gamma_d \bar{u}_c - \Gamma_{fg} u_i\right)\int_0^1 \left[P_{f,y}\int_0^{y/\delta}\frac{1}{P_{f,y}} d\left(\frac{y}{\delta}\right)\right] d\left(\frac{y}{\delta}\right)}{\int_0^1 \left[P_{f,y}\int_0^{y/\delta}\frac{A_{f,*}}{P_{f,y}} d\left(\frac{y}{\delta}\right)\right] d\left(\frac{y}{\delta}\right)}. \tag{36}$$

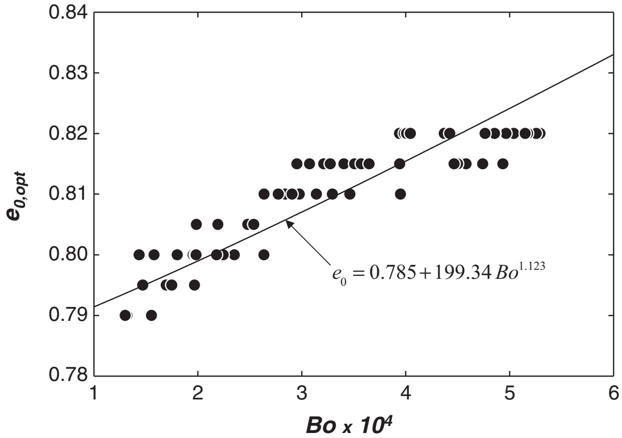

Fig. 6. Variation of optimal initial entrainment quality with boiling number.

The double integration terms in the numerator and denominator of Eq. (36) can be expanded for an arbitrary function $F(y)$ according to the relation

$$\int_0^1 \left[P_{f,y}\int_0^{y/\delta} F(y)\,d\left(\frac{y}{\delta}\right)\right]d\left(\frac{y}{\delta}\right) = 2(H_{ch}+W_{ch})\int_0^1\left[\int_0^{y/\delta} F(y)d\left(\frac{y}{\delta}\right)\right]d\left(\frac{y}{\delta}\right) - 4\delta\left[\int_0^1\left(1-\left(\frac{y}{\delta}\right)^2\right)F(y)d\left(\frac{y}{\delta}\right)\right], \quad (37)$$

which yields

$$\int_0^1 \left[P_{f,y}\int_0^{y/\delta} \frac{1}{P_{f,y}}d\left(\frac{y}{\delta}\right)\right]d\left(\frac{y}{\delta}\right) = 2(H_{ch}+W_{ch})\int_0^1\left[\int_0^{y/\delta} \frac{1}{P_{f,y}}d\left(\frac{y}{\delta}\right)\right]d\left(\frac{y}{\delta}\right) - 4\delta\left[\int_0^1\left(1-\left(\frac{y}{\delta}\right)^2\right)\frac{1}{P_{f,y}}d\left(\frac{y}{\delta}\right)\right] \quad (38)$$

and

$$\int_0^1 \left[P_{f,y}\int_0^{y/\delta} \frac{A_{f,*}}{P_{f,y}}d\left(\frac{y}{\delta}\right)\right]d\left(\frac{y}{\delta}\right) = 2(H_{ch}+W_{ch})\int_0^1\left[\int_0^{y/\delta} \frac{A_{f,*}}{P_{f,y}}d\left(\frac{y}{\delta}\right)\right]d\left(\frac{y}{\delta}\right) - 4\delta\left[\int_0^1\left(1-\left(\frac{y}{\delta}\right)^2\right)\frac{A_{f,*}}{P_{f,y}}d\left(\frac{y}{\delta}\right)\right]. \quad (39)$$

The next step in the model development is to apply momentum conservation to the mixture core control volume shown schematically in Fig. 7(b),

$$\frac{d\left(\int_\delta^y \rho_H u_H^2 P_{H,y}dy\right)}{dz}\Delta z + \Gamma_d \bar{u}_c \Delta z - \Gamma_{fg} u_i \Delta z = -\frac{d(pA_{H,*})}{dz}\Delta z - \tau_i P_{f,\delta}\Delta z + \tau_H P_{H,y}\Delta z + \left(p+\frac{1}{2}\left(\frac{dp}{dz}\right)\Delta z\right)\frac{dA_{H,*}}{dz}\Delta z. \quad (40)$$

where $P_{H,y}$ and $A_{H,*}$ are, respectively, the flow area and inner perimeter of the vapor core control volume, which are defined in Table 3. Re-arranging Eq. (40), neglecting $(\Delta z)^2$ term, yields the following relation for shear stress across the core,

$$\tau_H(y) = \frac{1}{P_{H,y}}\left[A_{H,*}\left(\frac{dp}{dz}\right) + \left(\Gamma_d \bar{u}_c - \Gamma_{fg} u_i + \tau_i P_{f,\delta}\right) + \frac{d}{dz}\left(\int_\delta^y \rho_H u_H^2 P_{H,y}dy\right)\right]. \quad (41)$$

Notice that, unlike the annular laminar liquid film, the core can acquire high axial velocity and is mostly turbulent. Therefore, shear stress across the core should also be expressed as

$$\tau_H(y) = \mu_H\left(1+\frac{\varepsilon_m}{\nu_H}\right)\frac{du_H}{dy}, \quad (42)$$

where ε_m is the eddy momentum diffusivity and ν_H the kinematic viscosity of the mixture, the latter is obtained using the following expression by Beattie and Walley [49],

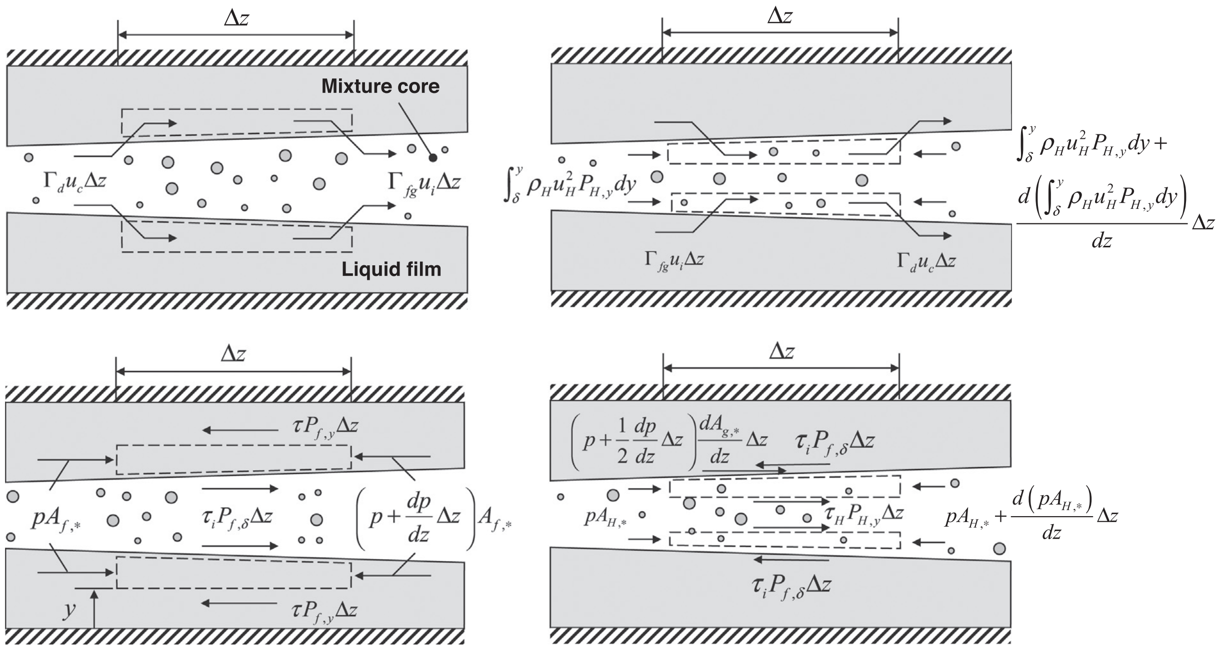

(a) (b)

Fig. 7. (a) Momentum and force components associated with liquid film control volume. (b) Momentum and force components associated with two-phase mixture core control volume.

Table 3
Geometrical parameters employed in the model's control volumes.

Core flow area, A_c	$A_c = (W_{ch} - 2\delta)(H_{ch} - 2\delta)$
Channel cross-sectional area, A_{ch}	$A_{ch} = W_{ch} H_{ch}$
Flow area of liquid control volume, $A_{f,*}$	$A_{f,*} = (W_{ch} - 2y)(H_{ch} - 2y) - (W_{ch} - 2\delta)(H_{ch} - 2\delta)$
Flow area of mixture core control volume, $A_{H,*}$	$A_{H,*} = (W_{ch} - 2\delta)(H_{ch} - 2\delta) - (W_{ch} - 2y)(H_{ch} - 2y)$
Effective vapor core hydraulic diameter, $D_{h,c}$	$D_{h,c} = \frac{4A_c}{P_{f,\delta}}$
Frictional perimeter, P_F	$P_F = 2(W_{ch} + H_{ch})$
Local perimeter in liquid film, $P_{f,y}$	$P_{f,y} = 2(H_{ch} - 2y) + 2(W_{ch} - 2y)$
Interfacial perimeter, $P_{f,\delta}$	$P_{f,\delta} = 2(H_{ch} - 2\delta) + 2(W_{ch} - 2\delta)$
Local perimeter in mixture core, $P_{H,y}$	$P_{H,y} = 2(H_{ch} - 2y) + 2(W_{ch} - 2y)$
Interfacial perimeter for core	$P_{H,\delta} = 2(H_{ch} - 2\delta) + 2(W_{ch} - 2\delta) = P_{f,\delta}$
Heated perimeter, P_H	$P_H = W_{ch} + 2H_{ch}$
Aspect ratio, β	$\beta = \frac{W_{ch}}{H_{ch}};\ \beta \leqslant 1$
Vapor core aspect ratio, β_c	$\beta_c = \frac{(W_{ch} - 2\delta)}{(H_{ch} - 2\delta)}$

$$\nu_H = \frac{1}{\rho_H}\left[\omega\mu_g + (1-\omega)(1+2.5\omega)\mu_f\right] \tag{43}$$

where

$$\omega = \frac{x_c v_g}{v_f + x_c v_{fg}}. \tag{44}$$

It should be noted that the expression by Beattie and Walley has been shown in a previous study by the authors [43] to provide good predictions of pressure drop when incorporated with the Homogeneous Equilibrium Model (HEM). Combining Eqs. (41) and (42) and integrating with respect to y, yield the following expression for velocity profile for the mixture core,

$$\begin{aligned} u_H(y) = \frac{1}{\mu_H}\Bigg[&\left(\frac{dp}{dz}\right)\int_\delta^y \frac{A_{H,*}}{P_{H,y}}\left(1+\frac{\varepsilon_m}{\nu_H}\right)^{-1} dy \\ &+ \left(\Gamma_d \bar{u}_c - \Gamma_{fg} u_i + \tau_i P_{f,\delta}\right)\int_\delta^y \left(\frac{1}{P_{H,y}}\right)\left(1+\frac{\varepsilon_m}{\nu_H}\right)^{-1} dy \\ &+ \int_\delta^y \frac{1}{P_{H,y}}\left(1+\frac{\varepsilon_m}{\nu_H}\right)^{-1}\frac{d}{dz}\left(\int_\delta^y \rho_H u_H^2 P_{H,y}\, dy\right) dy\Bigg] + u_i. \end{aligned} \tag{45}$$

To simplify analysis, the mixture momentum term $\int_\delta^y \rho_H u_H^2 P_{H,y} dy$ is approximated using a turbulent 1/7th power law velocity profile,

$$u_H(y) = u_{\max}\left(\frac{y-\delta}{(H_{ch}/2)-\delta}\right)^{1/7} + u_i, \tag{46}$$

which has been proven both experimentally and empirically to provide accurate approximations for turbulent pipe flows. The highest velocity, u_{max}, at the center of the core, is calculated by applying mass conservation to the mixture core,

$$\int_\delta^{H_2/2} \rho_H u_H P_{H,y}\, dy. \tag{47}$$

Noting that $W_{ch} = H_{ch}$ for the present square micro-channels, Eq. (47) yields

$$u_{\max} = \left[\frac{15}{49}\left(\frac{\dot{m}_H}{\rho_H}\right)\frac{1}{((H_{ch}/2)-\delta)^2} - \frac{60}{49}u_i\right], \tag{48}$$

where $\dot{m}_H = \dot{m}_g + \dot{m}_e$.

The mixture momentum term $\int_\delta^y \rho_H u_H^2 P_{H,y} dy$ can now be expressed as

$$\begin{aligned} \int_\delta^y \rho_H u_H^2 P_{H,y}\, dy = 4\rho_H\Bigg[&\frac{u_{H,\max}^2 H_{ch}}{(H_{ch}/2-\delta)^{2/7}} \times \frac{7}{9}(y-\delta)^{9/7} + \frac{2u_{H,max} u_i H_{ch}}{(H_{ch}/2-\delta)^{1/7}} \\ &\times \frac{7}{8}(y-\delta)^{8/7} + u_i^2 H_{ch}(y-\delta)\Bigg] \\ - 8\rho_H\Bigg[&\frac{u_{H,\max}^2}{(H_{ch}/2-\delta)^{2/7}} \times \frac{(y-\delta)^{9/7}\left(\frac{9}{7}y+\delta\right)}{\left(\frac{2}{7}+1\right)\left(\frac{2}{7}+2\right)} + \frac{2u_{H,max} u_i}{(H_{ch}/2-\delta)^{1/7}} \\ &\times \frac{(y-\delta)^{8/7}\left(\frac{8}{7}y+\delta\right)}{\left(\frac{1}{7}+1\right)\left(\frac{1}{7}+2\right)} + \frac{1}{2}(y^2-\delta^2)u_i^2\Bigg]. \end{aligned} \tag{49}$$

Setting $y = H/2$ and re-arranging Eq. (41) yield a relation for the interfacial shear stress obtained by momentum balance,

$$\tau_{i,mb} = \frac{1}{P_{f,\delta}}\left[A_c\left(-\frac{dp}{dz}\right) - \frac{d}{dz}\left(\int_\delta^{H/2} \rho_H u_H^2 P_{H,y}\, dy\right) - \Gamma_d u_c + \Gamma_{fg} u_i\right], \tag{50}$$

Wallis [71] recommended the following relation for interfacial shear in the presence of interfacial evaporation,

$$\tau_{i,Wallis} = \frac{1}{2} f_i \rho_H (\bar{u}_c - u_i)^2 - \frac{(\bar{u}_c - u_i)\Gamma_{fg}}{2P_{f,\delta}}, \tag{51}$$

which shows strong dependence on velocity difference between the mixture core and interface. The interfacial friction factor, f_i, in Eq. (51) is determined from empirical correlations for laminar flow [72],

$$f_i = \frac{24}{\mathrm{Re}_c}\left(1 - 1.3553\beta_c + 1.9467\beta_c^2 - 1.7012\beta_c^3 + 0.9564\beta_c^4 - 0.2537\beta_c^5\right) \quad \text{for } \mathrm{Re}_c < 2000, \tag{52}$$

and turbulent flow [73],

$$f_i = 0.079\mathrm{Re}_c^{-0.25} \text{ for } 2000 \leqslant \mathrm{Re}_c < 20{,}000, \tag{53a}$$

and

$$f_i = 0.046\mathrm{Re}_c^{-0.2} \text{ for } \mathrm{Re}_c \geqslant 20{,}000, \tag{53b}$$

where Re_c, $D_{h,c}$, and β_c are the mixture core's effective Reynolds number, hydraulic diameter and aspect ratio, which are defined, respectively, as

$$\mathrm{Re}_c = \frac{\rho_H(\bar{u}_c - u_i)D_{h,c}}{\mu_H}, \tag{54}$$

$$D_{h,c} = \frac{4A_c}{P_{f,\delta}}, \tag{55}$$

and

$$\beta_c = \frac{(W_{ch} - 2\delta)}{(H_{ch} - 2\delta)}. \tag{56}$$

3.2.2. Mixture core turbulence model

Applying linear approximation to shear stress across the mixture core, where $\tau_H = \tau_i$ at the interface, and $\tau_H = 0$ at the centerline, gives

$$\frac{\tau_H}{\tau_i} = \left(1 - \frac{y^+}{\delta_H^+}\right), \tag{57}$$

where

$$y^+ = \frac{y u^*}{\nu_H} \tag{58}$$

and

$$u^* = \left(\frac{\tau_i}{\rho_H}\right)^{0.5}. \tag{59}$$

Note that the dimensionless mixture core span, δ_H^+, ranges from $\delta u^*/\nu_H$ to $(H_{ch}/2)u^*/\nu_H$. Eq. (57) can also be expressed as

$$\frac{\tau_H}{\tau_i} = \left(1 + \frac{\varepsilon_m}{\nu_H}\right)\frac{du^+}{dy^+}, \tag{60}$$

where

$$u^+ = \frac{u}{u^*}. \tag{61}$$

An expression for eddy diffusivity is derived using an approach proposed by Kays [74] and Kays and Crawford [75]. Using Prandtl's mixing length theory, eddy momentum diffusivity, ε_m/ν_H, is expressed as the product of mixing length, l^+, and nondimensional velocity gradient, du^+/dy^+,

$$\frac{\varepsilon_m}{\nu_H} = l^{+2}\frac{du^+}{dy^+}. \tag{62}$$

Using the Van Driest function to account for turbulence damping at the interface, the mixing length is expressed as

$$l^+ = K\,y^+ D = K\,y^+\left[1 - \exp\left(-\sqrt{\frac{\tau_H}{\tau_i}}\frac{y^+}{A^+}\right)\right], \tag{63}$$

where $K = 0.4$ is von-Karman's constant, and the damping coefficient, A^+, is determined from experimental data [74,75],

$$A^+ = a\left(1 + b\mu_H\rho_H^{-0.5}\tau_i^{-1.5}\frac{dp}{dz}\right)^{-1}. \tag{64}$$

In the present study, the constant coefficients a and b in Eq. (64) are determined by aiming for minimum mean absolute error (MAE) when comparing predicted and experimental values of mass flow rate of mixture core, using Eq. (10) for $m_{g,\mathrm{exp}}$ and Eq. (22) for $m_{e,\mathrm{exp}}$, where

$$MAE\,(\%) = \frac{1}{N}\sum\left[\frac{\left|\dot{m}_{H,pred} - \dot{m}_{H,\mathrm{exp}}\right|}{\dot{m}_{H,\mathrm{exp}}} \times 100\right], \tag{65}$$

$$\dot{m}_{H,pred} = \int_y^{H_{ch}/2} \rho_H u_H P_{H,y}dy, \tag{66}$$

and

$$\dot{m}_{H,\mathrm{exp}} = \dot{m}_{g,\mathrm{exp}} + \dot{m}_{e,\mathrm{exp}}. \tag{67}$$

Fig. 8 shows the values $a = 26$ and $b = 28.18$ yield the smallest MAE of 12.9%.

Substituting Eqs. (60) and (63) into (62) yields the following relation for eddy diffusivity,

$$\frac{\varepsilon_m}{\nu_H} = -\frac{1}{2} + \frac{1}{2} \times \sqrt{1 + 4(K\,y^+)^2\left[1 - \exp\left(-\sqrt{\frac{\tau_H}{\tau_i}}\frac{y^+}{A^+}\right)\right]^2\left(1 - \frac{y^+}{\delta_H^+}\right)}. \tag{68}$$

Various relations for ε_m/ν_H have been suggested in prior studies [60,76,77] to capture the interfacial damping of turbulence. A recent study by Kim and Mudawar [60] showed better predictions are achieved by reducing the influence of surface tension at the interface by eliminating the term $(1 - y^+/\delta_H^+)$ from Eq. (68), which results in the final form used in the present model,

$$\frac{\varepsilon_m}{\nu_H} = -\frac{1}{2} + \frac{1}{2}\sqrt{1 + 4(K\,y^+)^2\left[1 - \exp\left(-\sqrt{\frac{\tau_H}{\tau_i}}\frac{y^+}{A^+}\right)\right]^2}. \tag{69}$$

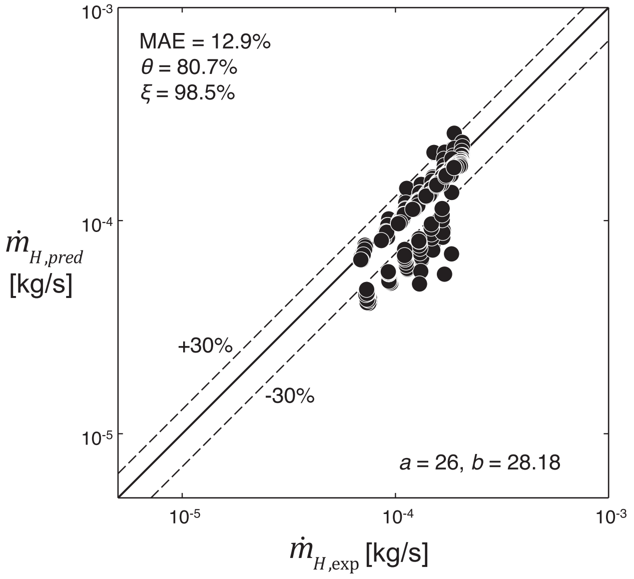

Fig. 8. Comparison of predicted and experimental core mass flow rates using mixing length damping coefficients $a = 26$ and $b = 28.18$.

3.2.3. Determination of heat transfer coefficient

For the laminar liquid film, temperature at distance of y from the heating wall can be calculated from heat flux, q'', across the liquid film [77],

$$\frac{q''}{q''_H} = \frac{1}{\mathrm{Pr}_f}\frac{dT^+}{dy^+}, \tag{70}$$

where q''_H is the heat flux along the heated perimeter of the channel, and dimensionless temperature and q''/q''_H are defined, respectively, by

$$T^+ = \frac{\rho_f c_{p,f} u_w^*(T_w - T)}{q''_H} \tag{71}$$

and

$$\frac{q''}{q''_H} = \frac{(W_{ch} + 2H_{ch})}{2(W_{ch} - 2y) + 2(H_{ch} - 2y)}, \tag{72}$$

where

$$u_w^* = \left(\frac{\tau_w}{\rho_f}\right)^{0.5} \tag{73}$$

and

$$y^+ = \frac{y u_w^*}{\nu_f}. \tag{74}$$

The local two-phase heat transfer coefficient, h_{tp}, is then calculated using the relation

$$h_{tp} = \frac{q''_H}{T_w - T_{sat}} = \frac{\rho_f c_{p,f} u_w^*}{T_\delta^+} = \frac{\rho_f c_{p,f} u_w^*}{\int_0^{\delta^+} \mathrm{Pr}_f \frac{q''}{q''_H}dy^+} = \frac{k_f}{\int_0^{\delta} \frac{(W_{ch}+2H_{ch})}{2(W_{ch}-2y)+2(H_{ch}-2y)}dy}. \tag{75}$$

3.3. Solution procedure

In the absence of an analytical scheme for evaluating the third term inside the bracket in Eq. (45),

$$\int_0^{\delta}\frac{1}{y}\int_o^{y} F(y)dydy, \tag{76}$$

a numerical iterative finite difference scheme is adopted to solve the model equations.

The length of channel is divided into small Δz segments, and the model calculations are performed from the axial location corresponding to onset of annular flow to the end of the channel or until saturated flow is sustained. Fig. 9 provides the detailed calculation procedure, which consists of the following steps:

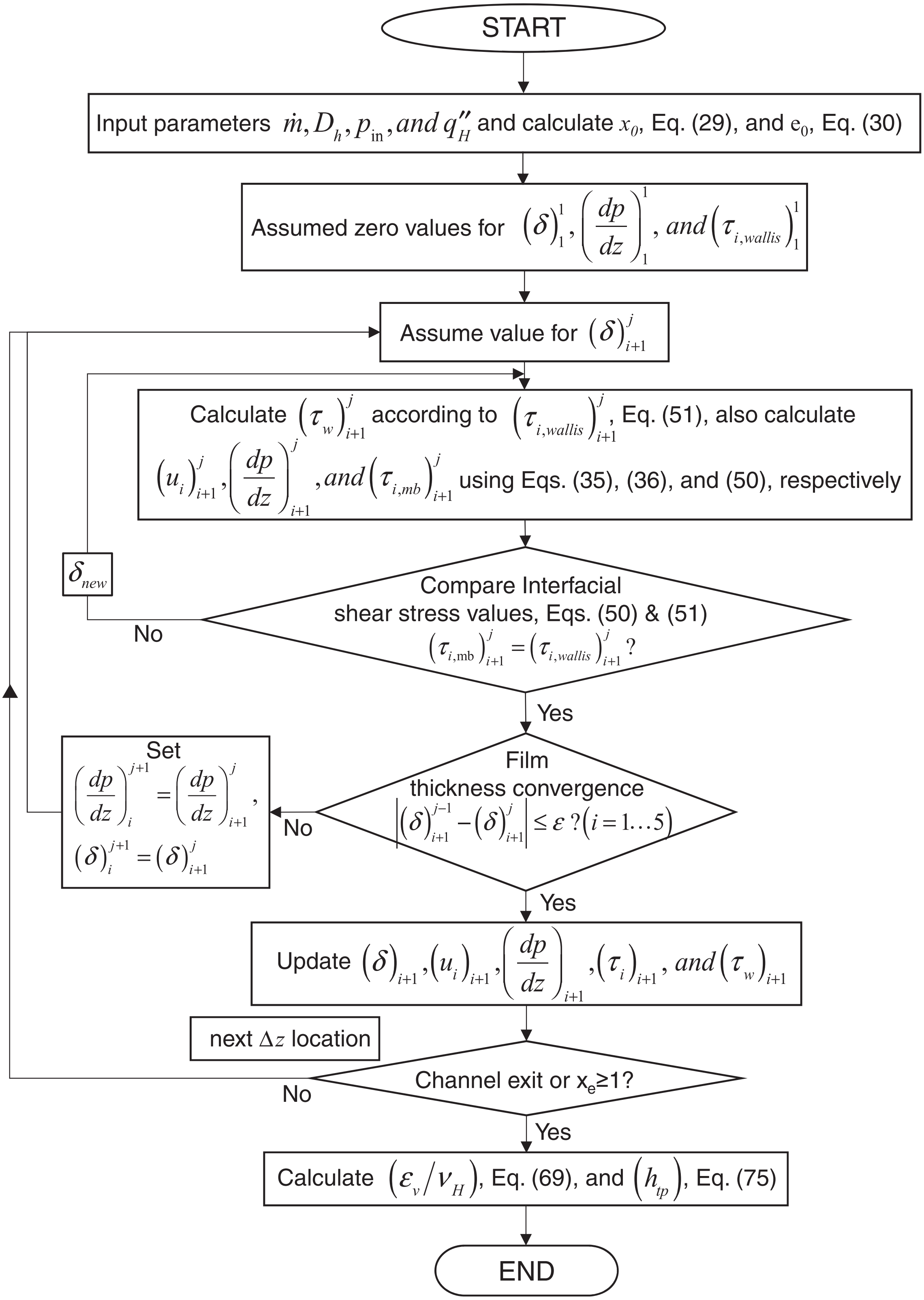

Fig. 9. Solution procedure for annular flow model.

(1) Mass flow rate, $\dot{m}$, hydraulic diameter, D_h, inlet pressure, p_{in}, and heat flux,q''_H, are provided as input parameters, and Eqs. (29) and (30) are used to calculate vapor quality, x_0, and entrained droplet quality, e_0, respectively, at the onset of annular flow.

(2) For initial iteration in the axial direction, $(\delta)_1^1$, $(dp/dz)_1^1$, and $(\tau_{i,wallis})_1^1$ are set to zero at the axial location corresponding to onset of annular flow. Here, i and j in $(\delta)_i^j$ represent spatial index and iteration number, respectively.

(3) The value of $(\delta)_{i+1}^j$ is assumed for the next Δz location in the range of $(1-\alpha)(\delta)_i \leqslant (\delta)_{i+1}^j \leqslant (1+\alpha)(\delta)_i$, with α ranging from 0.2 to 0.5, as axial iteration and refinement in δ estimation progress.

(4) Wall shear stress, $(\tau_w)_{i+1}^j$, is calculated using the interfacial shear stress relation by Wallis, $(\tau_{i,wallis})_{i+1}^j$, using Eq. (51). Then, interfacial velocity, $(u_i)_{i+1}^j$, pressure gradient,$(dp/dz)_{i+1}^j$, and interfacial shear stress by momentum balance, $(\tau_{i,mb})_{i+1}^j$, are calculated using Eqs. (35), (36), and (50), respectively.

(5) Convergence is checked by comparing $(\tau_{i,wallis})_{i+1}^j$ and $(\tau_{i,mb})_{i+1}^j$. If the two values are not equal, a new value for δ, using a small increment $\Delta\delta$, is used to re-calculate values in step (4). Steps (3) to (5) are repeated until a value for δ is found that renders the two shear stresses equal at location $(i+1)$.

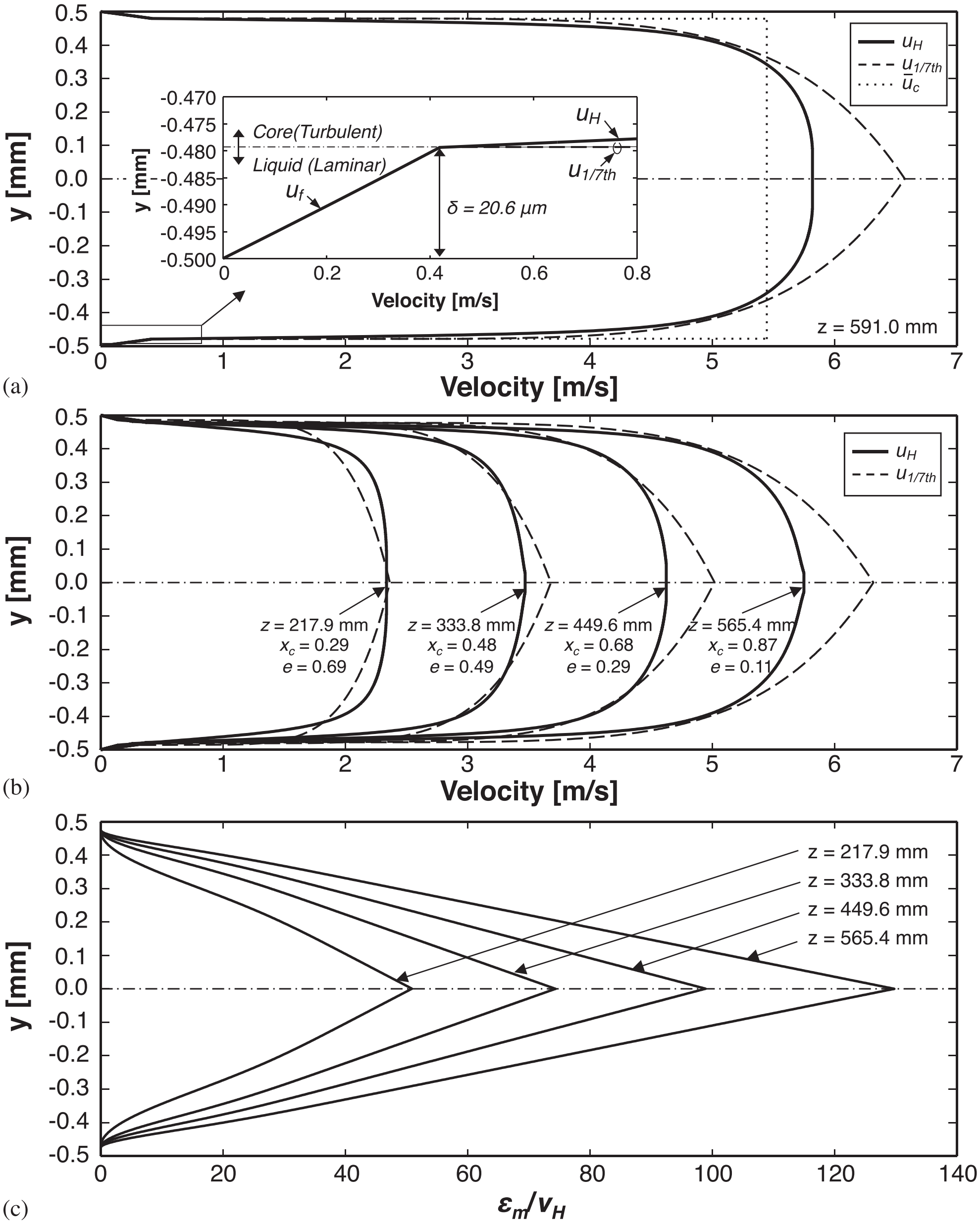

Fig. 10. Calculated annular flow results for G = 208.8 kg/m^{2}s and q''_B = 26,237 W/m^2: (a) Velocity profile at z = 591.0 mm compared to 1/7th power profile and constant velocity for mixture core. (b) Velocity profile compared with 1/7th power mixture core profile for four axial locations. (c) Eddy momentum diffusivity profile for mixture core for four axial locations.

(6) Calculated film thickness, $(\delta)_{i+1}^{j}$, is checked for convergence by comparing its value with that from the previous step, $(\delta)_{i+1}^{j-1}$, at five locations downstream from the onset of annular flow. Film thickness for locations farther downstream are calculated without this film thickness convergence test.

(7) Calculated $(\delta)_{i+1}^{j}$ and $(dp/dz)_{i+1}^{j}$ are used for the next step in axial iterations.

(8) Values for $(\delta)_{i+1}^{j}, (u_i)_{i+1}^{j}, (dp/dz)_{i+1}^{j}, (\tau_i)_{i+1}^{j}, (\tau_w)_{i+1}^{j}$ are updated at locations (i) and ($i+1$), and steps (3) to (8) are repeated until the end of the channel or as far as saturated flow is sustained.

(9) Mixture core eddy momentum diffusivity, ε_m/ν_H, and heat transfer coefficient, h_{tp}, are determined using Eqs. (69) and (75), respectively, over the entire axial calculation domain.

4. Model predictions and assessment

4.1. Velocity and eddy diffusivity profiles

Fig. 10(a) shows velocity profiles for the liquid film and mixture core calculated using Eqs. (34) and (45), respectively, at $z = 591.0$ mm for $G = 208.8$ kg/m^{2}s and $q''_B = 26{,}237$ W/m^2. Also shown for comparison are 1/7th power core mixture velocity, $u_{1/7th}$, and flat core velocity, $\bar{u}_c$. The calculate mixture core velocity, u_H, increases appreciably near the interface then more gradually, before reaching zero slope at the centerline, compared to an unrealistic pointed profile for $u_{1/7th}$ at the centerline. Most notable is large velocity difference between the liquid film and mixture core, which is manifest in high interfacial shear. The magnified velocity plot in Fig. 10(a) shows the flow changing from laminar in liquid

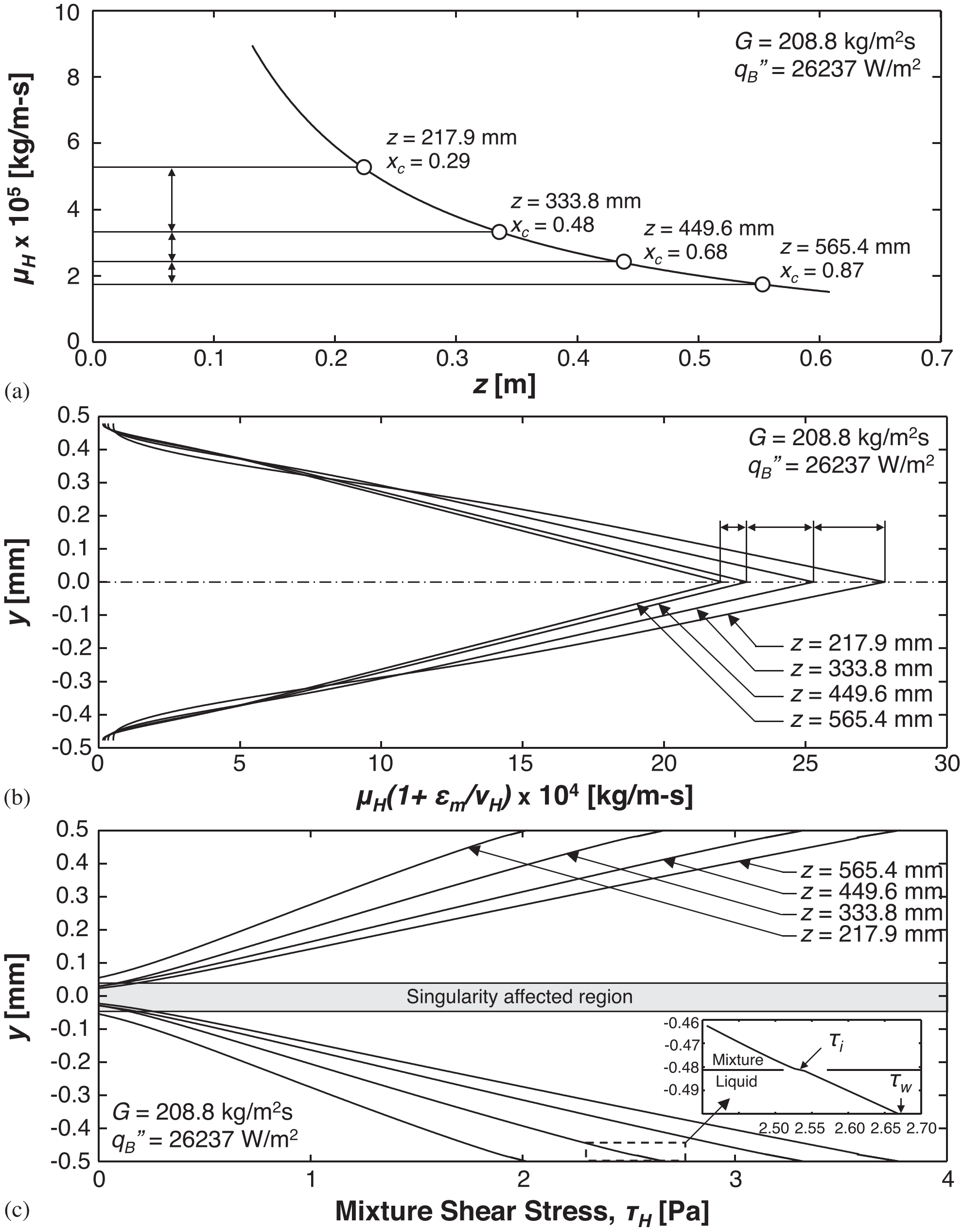

Fig. 11. Axial profile variations for (a) mixture viscosity, μ_H, (b) $\mu_H(1 + \varepsilon_m/\nu_H)$, and (c) mixture core shear stress, τ_H, at four axial locations for $G = 208.8$ kg/m^{2}s and $q''_B = 26{,}237$ W/m^2.

film to turbulent in the mixture core. The annular liquid film thickness, δ, for this case is calculated as 20.6 µm.

Fig. 10(b) shows calculated velocity profiles, u_f and u_H, along with $u_{1/7th}$ at four axial locations. Notice that the u_H profile is flatter upstream, and centerline differences between u_H and $u_{1/7th}$ increase along the channel. Fig. 10(c) shows eddy momentum diffusivity of the mixture core, ε_m/ν_H, increases in magnitude along the channel, which is the outcome of increased flow rate and therefore greater turbulence in the mixture core. Effects of interfacial damping, which causes the core's eddy momentum diffusivity to drop to zero at the interface, are clearer for the upstream case, z = 217.9 mm.

It is important to note that axial variation of mixture viscosity, μ_H, has significant impact on velocity profile of the mixture core, u_H. Fig. 11(a) shows, for G = 208.8 kg/m^{2}s and q''_B = 26,237 W/m^2, μ_H decreases appreciably upstream, in the low x_c region, and more mildly downstream, in the high x_c region. This implies the impact of declining μ_H on u_H is more significant upstream because of higher shear offering greater resistance to velocity profile changes. Fig. 11(b) shows combined viscosity in the Boussinesq approximated form, $\mu_H(1+\varepsilon_m/\nu_H)$, decreases along the channel, a trend opposite to that for ε_m/ν_H captured in Fig. 10(c). The impact of the variation in Fig. 11(b) on du_H/dy is reflected in the relation

$$\frac{du_H}{dy} = \frac{\tau_H(y)}{\mu_H\left(1+\frac{\varepsilon_m}{\nu_H}\right)}, \tag{77}$$

where τ_H is the mixture core shear stress. Fig. 11(c) shows variations of τ_H profile along the channel. Notice that shear stress across the film, τ_f, decreases from τ_w at the wall to τ_i at the interface, and shear stress across the core, τ_H, from τ_i to zero along the centerline, as shown in the inset in Fig. 11(c). For the downstream location, z = 565.4 mm, small μ_H causes the velocity profile to undergo more appreciable changes across the core, Fig. 10(b), compared to upstream locations. Smaller value of τ_H upstream also contributes

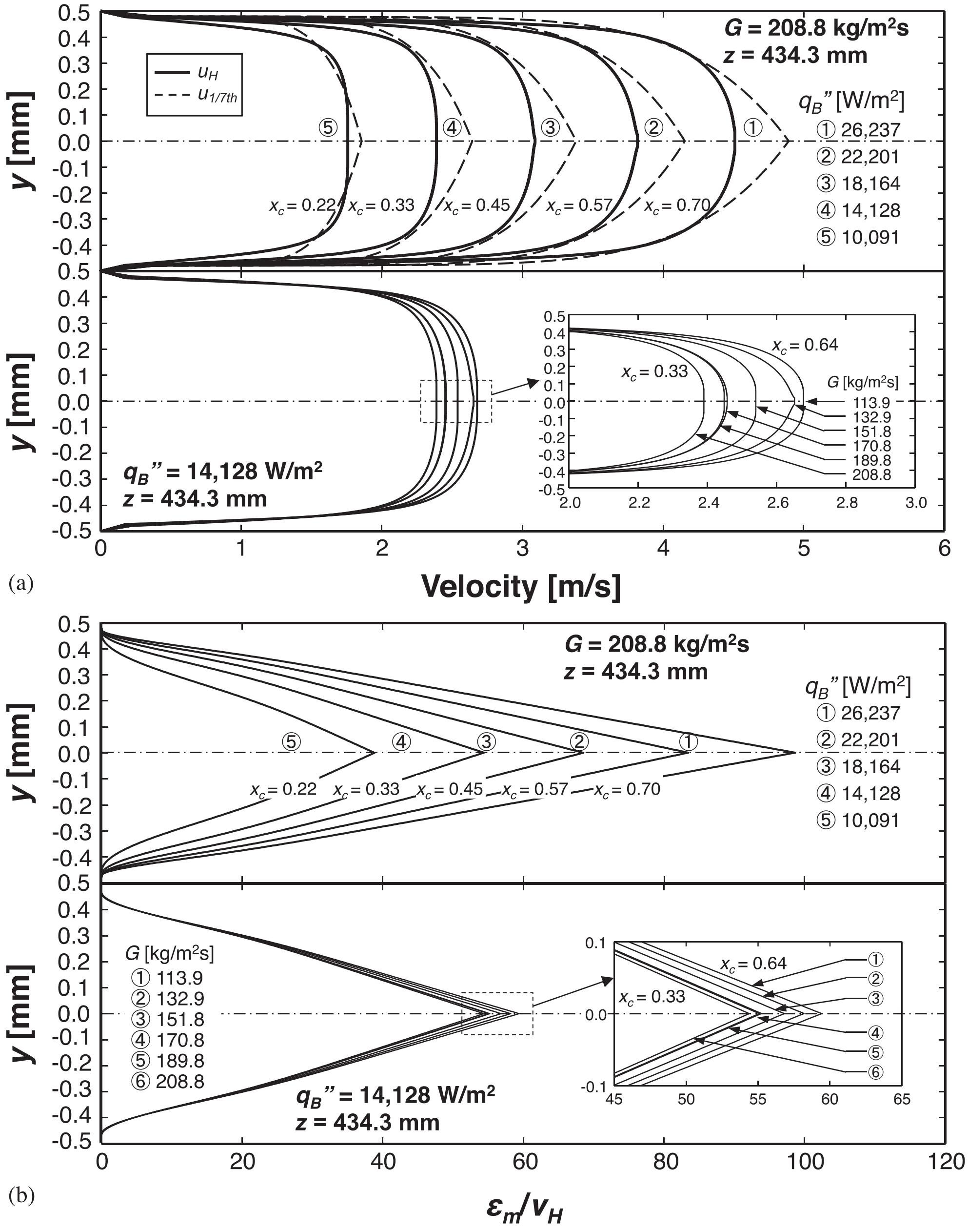

Fig. 12. Effects of heat flux and mass velocity on (a) velocity profile, and (b) eddy momentum diffusivity at z = 434.3 mm.

to flatter profile across the core. Calculation of core shear stress, τ_H, becomes unstable in the vicinity of the centerline because of a singularity in the term $1/P_{H,y} = 1/[2(H_{ch}-2y)+2(W_{ch}-2y)]$ for $y = H_{ch}/2 = W_{ch}/2$ in Eq. (41), which results in large deviations in the magnitude of τ_H corresponding to even small changes in the value calculated from terms inside the bracket of Eq. (41).

Fig. 12(a) and (b) show, for z = 434.3 mm, the influences of heat flux and mass velocity on velocity profile and eddy momentum diffusivity profile, respectively. Fig. 12(a) shows, for G = 208.8 kg/m^{2}s, appreciable core fluid acceleration resulting from increasing heat flux, whose magnitude is reflected in that of mixture quality. The same figure shows, for q''_B = 14,128 W/m^2, similar acceleration resulting from increasing mass velocity. Fig. 12(b) shows, for G = 208.8 kg/m^{2}s, appreciable increase in eddy diffusivity with increasing heat flux. This increase is the outcome of increasing mixing length, $l^+ = Ky^+D$, resulting from increased τ_i and decreased μ_H, according to Eqs. (58) and (59). Fig. 12(b) also shows, for q''_B = 14,128 W/m^2, that eddy diffusivity changes only slightly with increasing G, as the increase in ε_m/ν_H with increasing G is offset by increasing μ_H.

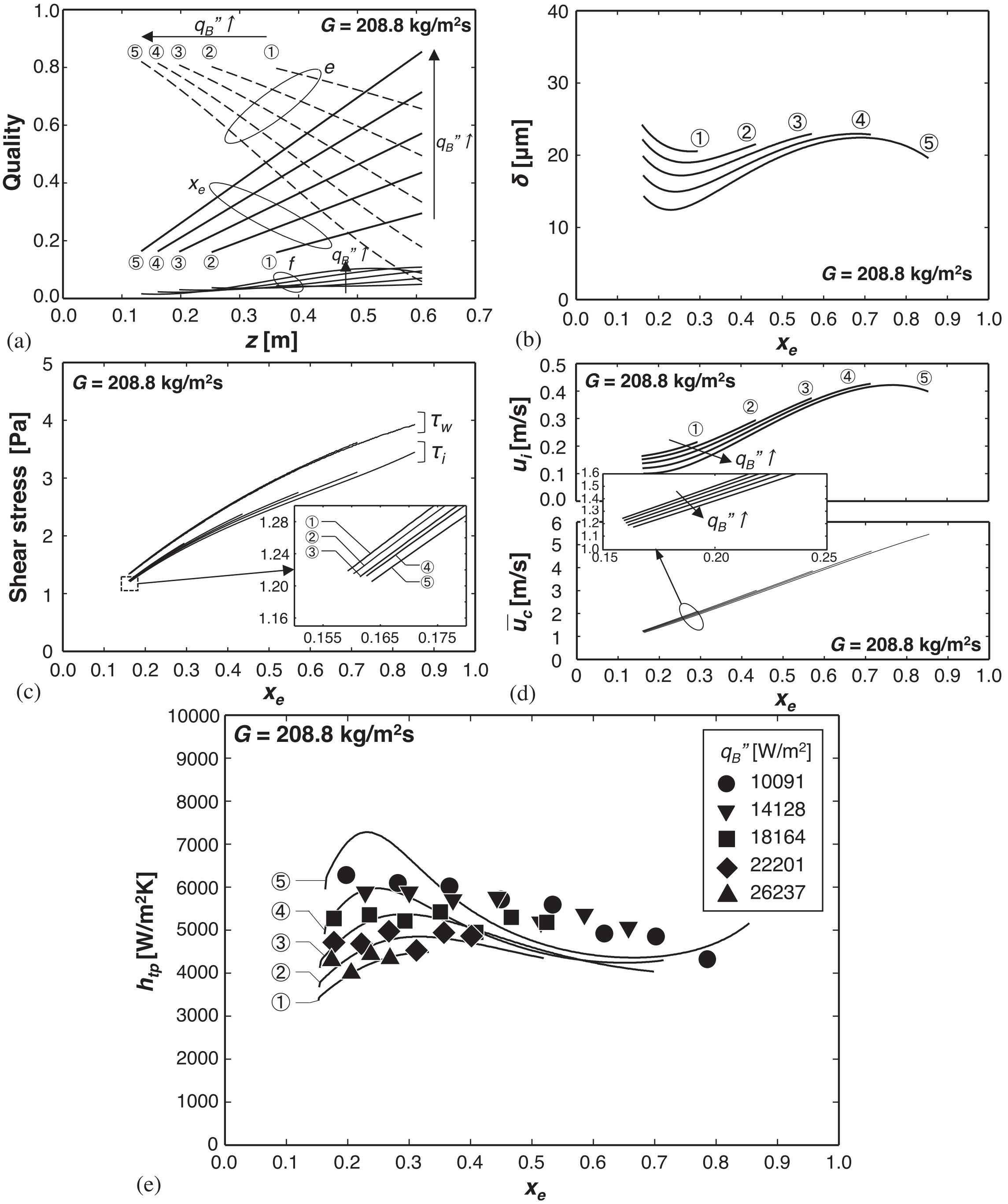

Fig. 13. Predicted variations of (a) quality versus axial distance, (b) liquid film thickness versus quality, (c) interfacial and wall shear stresses versus quality, and (d) interfacial and mixture core velocities versus quality, and (e) comparison of predicted and measured local two-phase heat transfer coefficients versus quality. Conditions for the cases shown are G = 208.8 kg/m^{2}s and ① q''_B = 10,091 W/m^2, ② q''_B = 14,128 W/m^2, ③ q''_B = 18,164 W/m^2, ④ q''_B = 22,201 W/m^2, and ⑤ q''_B = 26,237 W/m^2.

4.2. Variations of other flow parameters

Fig. 13(a)–(e) show predicted variations of several key parameters with increasing q''_B for a fixed mass velocity of $G = 208.8$ kg/m^{2}s; Fig. 13(e) also compares predicted and measured values of two-phase heat transfer coefficient. Fig. 13(a) shows location of onset of annular flow is shifted farther upstream with increasing q''_B. Fig. 13(a) also shows linear variation of vapor quality, x_e, along the channel, which also increases with increasing q''_B. In the same figure, entrained droplet quality, e, decreases along the channel, and deposition rate, represented by the slope of e relative to z, increases with increasing q''_B. The film quality, f, increases along the channel when deposition rate is greater than evaporation rate, and decreases in the downstream region where evaporation rate becomes stronger. Fig. 13(b) shows annular film thickness follows the trend of f along the channel, with initial thinning following the onset of annular flow, followed by film thickening because of droplet deposition, before thinning again due to stronger evaporation downstream. Fig. 13(c) shows both interfacial shear stress, τ_i, and wall shear stress, τ_w, increase monotonically along the channel. Increased magnitude of $(-dp/dz)$ with increasing q''_B accounts for the small albeit increasing difference between τ_w and τ_i. Notice

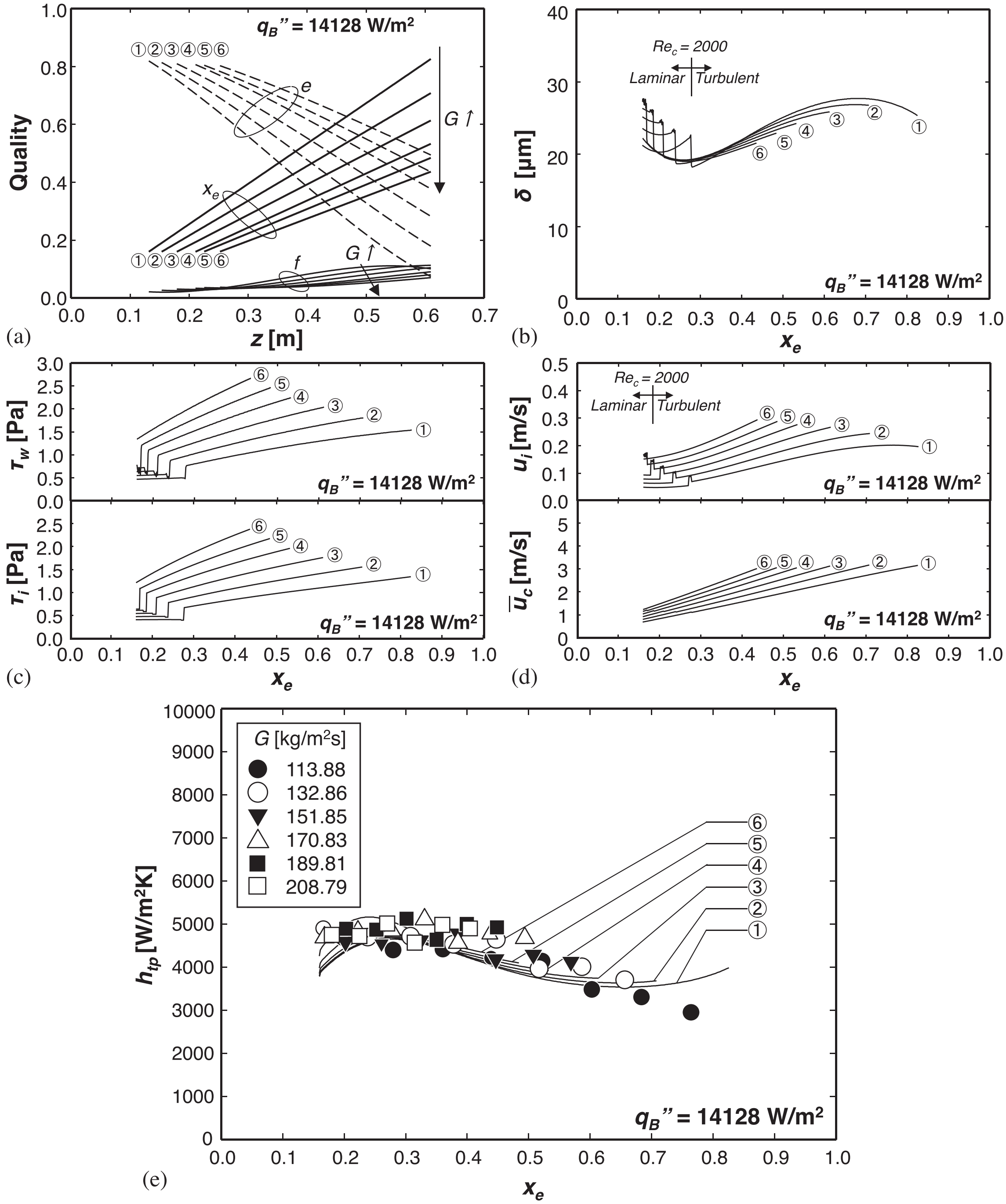

Fig. 14. Predicted variations of (a) quality versus axial distance, (b) liquid film thickness versus quality, (c) interfacial and wall shear stresses versus quality, and (d) interfacial and mixture core velocities versus quality, and (e) comparison of predicted and measured local two-phase heat transfer coefficients versus quality. Conditions for the cases shown are $q''_B = 14{,}128$ W/m^2 and ① $G = 113.88$ kg/m^{2}s, ② $G = 132.86$ kg/m^{2}s, ③ $G = 151.85$ kg/m^{2}s, ④ $G = 170.83$ kg/m^{2}s, ⑤ $G = 189.81$ kg/m^{2}s, and ⑥ $G = 208.79$ kg/m^{2}s.

that, at the onset of annular flow, τ_w and τ_i both decrease with increasing q''_B because of larger cross-sectional area, A_c, larger perimeter, $P_{f,\delta}$, and higher $(-dp/dz)$ as reflected by Eq. (32). Fig. 13(d) shows both interfacial velocity, u_i, and mean core velocity, $\bar{u}_c$, increase with increasing quality because of the axial decrease in core density, ρ_H, but the increase in u_i subsides downstream where evaporation becomes more dominant than deposition rate, which also increases core cross sectional area, A_c. In the same figure, u_i in the upstream region is shown decreasing with increasing q''_B because of smaller liquid film thickness, δ, and larger cross-sectional, A_c. Fig. 13(e) shows the model provides good predictions of local two-phase heat transfer coefficient, h_{tp}, along the flow direction for the different values of q''_B tested. Notice also that predictions are better able to capture the measured trend in the upstream region where nucleate boiling is dominant.

Fig. 14(a)–(e) show predicted variations of several key parameters with increasing G for a fixed heat flux of $q''_B = 14{,}128\ \mathrm{W/m^2}$; Fig. 14(e) also compares predicted and measured values of the two-phase heat transfer coefficient. Fig. 14(a) shows location of onset of annular flow is shifted downstream with increasing G. Entrained droplet quality, e, decreases along the channel as deposition rate, Γ_d, which is represented by the slope of e relative to z, increases with decreasing G. Fig. 14(b) shows the variation of δ with x_e is strongly demarcated by the transition from laminar to turbulent flow, as the interfacial friction factor, f_i, in $\tau_{i,wallis}$ increases once mixture core Reynolds number surpasses $Re_c = 2000$. Notice the thinning in δ with increasing G, which is the direct result of increased interfacial shear with increasing G. Fig. 14(c) shows τ_w and τ_i increase almost linearly along the channel as well as with increasing G. Fig. 14(d) shows $\bar{u}_c$ and u_i also increase along the channel because of decreasing ρ_H, but the increase in u_i abates downstream and even decreases for the lowest mass velocity as evaporation becomes more dominant than deposition rate. Fig. 14(e) shows the model provides good predictions of h_{tp} along the flow direction for the different values of G tested.

4.3. Overall assessment of the model predictions

The model predictions are compared to experimental data and assessed using mean absolute error, which is defined for pressure drop across the test module and local two-phase heat transfer coefficient, respectively, as

$$MAE(\%) = \frac{1}{N}\sum\left[\frac{\left|\Delta p_{pred} - \Delta p_{\exp}\right|}{\Delta p_{\exp}} \times 100\right] \tag{78a}$$

and

$$MAE(\%) = \frac{1}{N}\sum\left[\frac{\left|h_{pred} - h_{\exp}\right|}{h_{\exp}} \times 100\right]. \tag{78b}$$

In comparing predicted to measured pressure drop, total pressure drop, Δp, is calculated as the sum of components representing inlet contraction, Δp_c, upstream single-phase liquid region, $\Delta p_{sf,f}$, saturated boiling region preceding the onset of annular flow, $\Delta p_{tp,cor}$, saturated annular flow region, $\Delta p_{tp,ann}$, and exit expansion, Δp_e,

$$\Delta p = \Delta p_c + \Delta p_{sp,f} + \left(\Delta p_{tp,cor} + \Delta p_{tp,ann}\right) + \Delta p_e, \tag{79}$$

where $\Delta p_{tp,cor}$ is comprised of a frictional component, $\Delta p_{tp,F}$, and accelerational component, $\Delta p_{tp,A}$,

$$\Delta p_{tp,cor} = \left(\Delta p_{tp,F} + \Delta p_{tp,A}\right). \tag{80}$$

Notice that the present model concerns only the saturated annular flow region. The saturated two-phase pressure drop for the region preceding the onset of annular flow is calculated using Eq. (80), based on empirical correlations by Qu [58] for frictional pressure drop multiplier, ϕ_f^2, in

$$\left(\frac{dp}{dz}\right)_F = \left(\frac{dp}{dz}\right)_f \phi_f^2, \tag{81}$$

and with the accelerational pressure drop, $\Delta p_{tp,A}$, based on a void fraction relation by Zivi [78],

$$\alpha = \left[1 + \left(\frac{\rho_g}{\rho_f}\right)^{2/3}\left(\frac{1-x_e}{x_e}\right)\right]^{-1}. \tag{82}$$

Pressure drop for the saturated annular flow region is calculated using the present model according to

$$\Delta p_{tp,ann} = p_{0,ann} + \sum_{i=1}^{N} (dp/dz)_i \Delta z, \tag{83}$$

where $p_{0,ann}$ is pressure at the onset of annular flow calculated from pressure drops for the upstream regions.

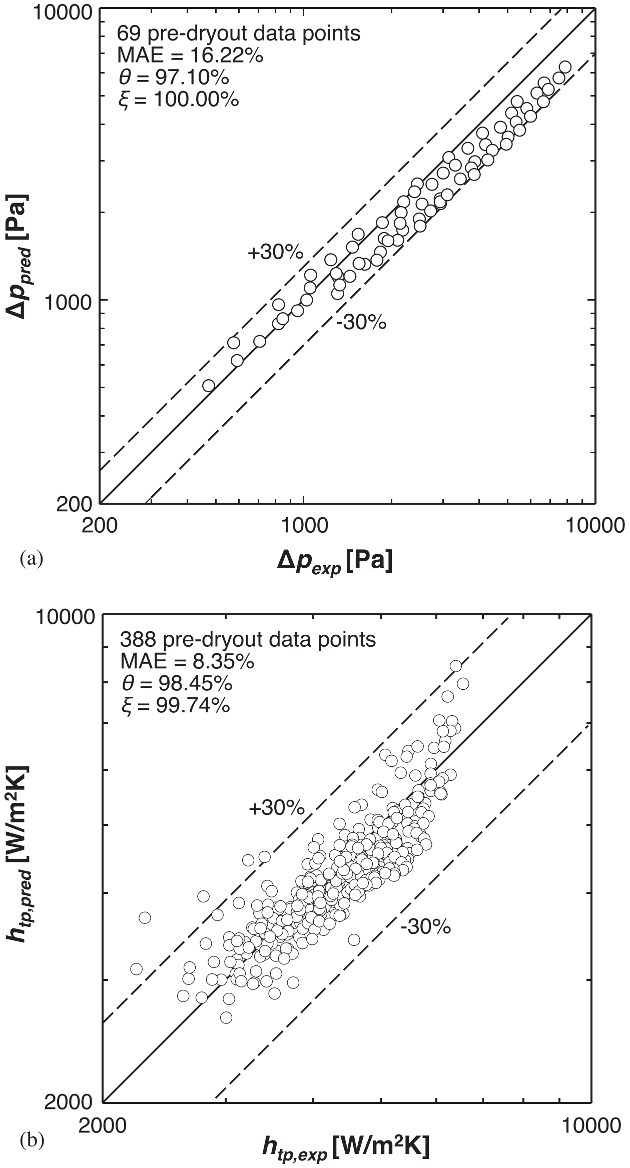

Fig. 15. Comparison of annular flow model predictions with experimental data for (a) pressure drop and (b) local heat transfer coefficient for pre-dryout annular flow.

Fig. 15(a) shows the model provides very good predictions of pressure drop, evidenced by a MAE for 69 data points of 16.22%, with $\theta = 97.10\%$ and $\xi = 100.00\%$ of the data falling within 30% and 50% of the data, respectively.

Fig. 15(b) shows the annular flow model is equally successful at predicting local heat transfer coefficient, with a MAE for 388 predryout data points of 8.35%, and with $\theta = 98.45\%$ and $\xi = 99.74\%$ of the data predicted within 30% and 50% of the data, respectively.

Despite good predictive capability against the present data, the model can benefit from further improvement in ability to tackle different fluids and broad ranges of inlet pressure, mass velocity, heat flux, aspect ratio, and length-to-diameter ratio. Reliance on broader parameter ranges can also facilitate development of more accurate relations for initial entrainment, e_0, and deposition coefficient, k. Future experimental work must also include direct measurement of droplet entrainment mass flow rate, $\dot{m}_e$, (see [68]) to enable accurate determination of local droplet quality, e_z, which would ultimately lead to better theoretical determination of film thickness. Modeling of annular liquid film would also benefit from direct measurements using high speed video [79] and thickness probes [80]. But perhaps most beneficial for development of annular flow models is detailed PIV measurement [81] of both velocity and turbulence in the core.

5. Conclusions

This study investigated pressured drop and heat transfer characteristics for saturated flow boiling in micro-channel heat sinks specific to the annular flow regime. The control volume method was employed to construct a theoretical model for annular flow, including new relations for liquid droplet entrainment and deposition. Unlike prior annular flow models, the present model includes detailed assessment of turbulence effects in the vapor core, enabling the development of detailed cross-sectional profiles for momentum diffusivity, velocity, and shear stress. Predictive accuracy of the model was assessed against experimental data for R134a using a 609.6-mm long and 203.2-mm wide micro-channel heat sink containing 100 of 1 × 1-mm^2 flow channels. Followings are key conclusions drawn from the study.

1. New empirical relations were developed for initial droplet entrainment at the onset of annular flow, as well as gradual droplet deposition along the channels.
2. A detailed model of the vapor core was provided which accounts for entrained liquid droplets, core mixture density and viscosity, and variations of eddy momentum diffusivity both across and along the channels. The eddy diffusivity profiles account for damping of turbulence along the liquid vapor interface.
3. The model shows good accuracy against 69 experimental pressure drop data points, with MAE of 16.22%, and 97.10% and 100.0% of the data predicted within 30% and 50%, respectively.
4. The model also shows good accuracy against 388 data points for local two-phase heat transfer coefficient, evidenced by a MAE of 8.35%, and with 98.45% and 99.74% of the data predicted within 30% and 50%, respectively.

Conflict of interest

The author declare that there is no conflict of interest.

Acknowledgement

The authors are grateful for the support of the National Aeronautics and Space Administration (NASA) under grant NNX17AK98G.

Appendix A. Supplementary material

Supplementary data associated with this article can be found, in the online version, at https://doi.org/10.1016/j.ijheatmasstransfer.2018.12.074.

References

[1] L.-T. Yeh, Review of heat transfer technologies in electronic equipment, J. Electronic Packaging 117 (1995) 333–339.
[2] I. Mudawar, Assessment of high-heat-flux thermal management schemes, IEEE Trans-CPMT 24 (2001) 122–141.
[3] R.R. Schmidt, B.D. Notohardjono, High-end server low-temperature cooling, IBM J. Res. Dev. 46 (2002) 739–751.
[4] R.C. Chu, The challenge of electronic cooling: past, current and future, J. Electronic Packaging 126 (2005) 491–500.
[5] I. Mudawar, T.M. Anderson, Parametric investigation into the effects of pressure, subcooling, surface augmentation and choice of coolant on pool boiling in the design of cooling systems for high-power density chips, J. Electronic Packaging 112 (1990) 375–382.
[6] J.D. Bernardin, I. Mudawar, A cavity activation and bubble growth model of the Leidenfrost point, J. Heat Transfer 124 (2002) 864–874.
[7] J.A. Shmerler, I. Mudawar, Local evaporative heat transfer coefficient in turbulent free-falling liquid films, Int. J. Heat Mass Transfer 31 (1988) 731–742.
[8] T.H. Lyu, I. Mudawar, Statistical investigation of the relationship between interfacial waviness and sensible heat transfer to a falling liquid film, Int. J. Heat Mass Transfer 34 (1991) 1451–1464.
[9] C.O. Gersey, I. Mudawar, Effects of heater length and orientation on the trigger mechanism for near-saturated flow boiling CHF – I. Photographic and statistical characterization of the near-wall interfacial features, Int. J. Heat Mass Transfer 38 (1995) 629–642.
[10] J.C. Sturgis, I. Mudawar, Critical heat flux in a long, rectangular channel subjected to one-sided heating – II. Analysis of CHF data, Int. J. Heat Mass Transfer 42 (1999) 1849–1862.
[11] W. Qu, I. Mudawar, Thermal design methodology for high-heat-flux single-phase and two-phase micro-channel heat sinks, IEEE Trans-CPMT 26 (2003) 598–609.
[12] S. Mukherjee, I. Mudawar, Pumpless loop for narrow channel and micro-channel boiling from vertical surfaces, J. Electronic Packaging 125 (2003) 431–441.
[13] I. Mudawar, D.C. Wadsworth, Critical heat flux from a simulated electronic chip to a confined rectangular impinging jet of dielectric liquid, Int. J. Heat Mass Transfer 34 (1991) 1465–1480.
[14] M.E. Johns, I. Mudawar, An ultra-high power two-phase jet-impingement avionic clamshell module, J. Electronic Packaging 118 (1996) 264–270.
[15] W.P. Klinzing, J.C. Rozzi, I. Mudawar, Film and transition boiling correlations for quenching of hot surfaces with water sprays, J. Heat Treating 9 (1992) 91–103.
[16] M. Visaria, I. Mudawar, Application of two-phase spray cooling for thermal management of electronic devices, IEEE Trans.-CPMT 32 (2009) 784–793.
[17] M.K. Sung, I. Mudawar, Single-phase hybrid micro-channel/jet impingement cooling, Int. J. Heat Mass Transfer 51 (2008) 4342–4352.
[18] I. Mudawar, Recent advances in high-flux, two-phase thermal management, J. Therm. Sci. Eng. Appl. 5 (2013) 021012.
[19] I. Mudawar, Two-phase micro-channel heat sinks: theory, applications and limitations, J. Electronic Packaging 133 (2011) 041002–41012.
[20] D.B. Tuckerman, R.F.W. Pease, High-performance heat sinking for VLSI, IEEE Electron Device Lett. 2 (1981) 126–129.
[21] R.J. Phillips, Micro-channel heat sinks, in: A. Bar-Cohen, A.D. Kraus (Eds.), Advances in thermal modeling of electronic components, ASME Press, New York, 1990, pp. 109–184.
[22] T.S. Ravigururajan, J.Cuta, C.E. McDonald, M.K. Drost, Single-phase flow thermal performance characteristics of a parallel micro-channel heat exchanger, National Heat Transfer Conf., vol. 7, ASME HTD-329, 1996, pp. 157–166.
[23] A.G. Fedorov, R. Viskanta, Three-dimensional conjugate heat transfer in the microchannel heat sink for electronic packaging, Int. J. Heat Mass Transfer 43 (2000) 399–415.
[24] M.B. Bowers, I. Mudawar, High flux boiling in low flow rate, low pressure drop mini-channel and micro-channel heat sinks, Int. J. Heat Mass Transfer 37 (1994) 321–332.
[25] M.B. Bowers, I. Mudawar, Two-phase electronic cooling using mini-channel and micro-channel heat sinks – part 1. Design criteria and heat diffusion constraints, J. Electronic Packaging 116 (1994) 290–297.
[26] M.B. Bowers, I. Mudawar, Two-phase electronic cooling using mini-channel and micro-channel heat sinks – part 2. Flow rate and pressure drop constraints, J. Electronic Packaging 116 (1994) 298–305.
[27] F.P. Chiaramonte, J.A. Joshi, Workshop on critical issues in microgravity fluids, transport, and reaction processes in advanced human support technology – final report, NASA Report TM-2004-212940, 2004.
[28] The National Academies, Recapturing a Future for Space Exploration: Life and Physical Sciences Research for a New Era, National Academies Press, Washington, DC, 2011.

[29] G.B. Ganapathi, G. Birur, E. Sunada, J. Miller, Two phase vs. single phase thermal loop trades for exploration mission LAT II architecture, SAE Paper 2008-01-1958, 2008.

[30] H. Zhang, I. Mudawar, M.M. Hasan, Experimental and theoretical study of orientation effects on flow boiling CHF, Int. J. Heat Mass Transfer 45 (2002) 4463–4478.

[31] H. Zhang, I. Mudawar, M.M. Hasan, Flow boiling CHF in microgravity, Int. J. Heat Mass Transfer 48 (2005) 3107–3118.

[32] C. Konishi, I. Mudawar, Review of flow boiling and critical heat flux in microgravity, Int. J. Heat Mass Transfer 80 (2015) 469–493.

[33] I. Mudawar, Flow boiling and flow condensation in reduced gravity, Adv. Heat Transfer 49 (2017) (2017) 225–306.

[34] S.H. Lee, I. Mudawar, M.M. Hasan, Thermal analysis of hybrid single-phase, two-phase and heat pump thermal control system (TCS) for future spacecraft, Appl. Therm. Eng. 100 (2016) 190–214.

[35] S. Lee, I. Mudawar, Investigation of flow boiling in large micro-channel heat exchangers in a refrigeration loop for space applications, Int. J. Heat Mass Transfer 97 (2016) 110–129.

[36] S. Lee, I. Mudawar, Transient characteristics of flow boiling in large micro-channel heat exchangers, Int. J. Heat Mass Transfer 103 (2016) 186–202.

[37] S. Lee, V.S. Devahdhanush, I. Mudawar, Investigation of subcooled and saturated boiling heat transfer mechanisms, instabilities, and transient flow regime maps for large length-to-diameter ratio micro-channel heat sinks, Int. J. Heat Mass Transfer 123 (2018) 172–191.

[38] S.M. Kim, I. Mudawar, Universal approach to predicting two-phase frictional pressure drop for mini/micro-channel saturated flow boiling, Int. J. Heat Mass Transfer 58 (2013) 718–734.

[39] S.M. Kim, I. Mudawar, Universal approach to predicting saturated flow boiling heat transfer in mini/micro-channels part I. Dryout incipience quality, Int. J. Heat Mass Transfer 64 (2013) 1226–1238.

[40] S.M. Kim, I. Mudawar, Universal approach to predicting saturated flow boiling heat transfer in mini/micro-channels – part II. Two-phase heat transfer coefficient, Int. J. Heat Mass Transfer 64 (2013) 1239–1256.

[41] S.M. Kim, I. Mudawar, Review of databases and predictive methods for heat transfer in condensing and boiling mini/micro-channel flows, Int. J. Heat Mass Transfer 77 (2014) 627–652.

[42] S.M. Kim, I. Mudawar, Review of two-phase critical flow models and investigation of the relationship between choking, premature CHF, and CHF in micro-channel heat sinks, Int. J. Heat Mass Transfer 87 (2015) (2015) 497–511.

[43] S. Lee, V.S. Devahdhanush, I. Mudawar, Pressure drop characteristics of large length-to-diameter two-phase micro-channel heat sinks, Int. J. Heat Mass Transfer 115 (2017) 1258–1275.

[44] W.H. McAdams, W.K. Woods, L.C. Heroman, Vaporization inside horizontal tubes, II. Benzene-oil mixture, Trans. ASME 64 (1942) 193–200.

[45] W.W. Akers, H.A. Deans, O.K. Crosser, Condensing heat transfer within horizontal tubes, Chem. Eng. Prog. 54 (1958) 89–90.

[46] A. Cicchitti, C. Lombardi, M. Silvestri, G. Soldaini, R. Zavalluilli, Two-phase cooling experiments-pressure drop, heat transfer and burnout measurements, Energia Nucleare 7 (1960) 407–425.

[47] W.L. Owens, Two-phase pressure gradient. Int. Dev. Heat Transfer, Pt. II., ASME, New York, 1961.

[48] A.E. Dukler, M. Wicks, R.G. Cleaveland, Pressure drop and hold up in two-phase flow, AIChE J. 10 (1964) 38–51.

[49] D.R.H. Beattie, P.B. Whalley, A simple two-phase frictional pressure drop calculation method, Int. J. Multiphase Flow 8 (1982) 83–87.

[50] G.M. Lazarek, S.H. Black, Evaporative heat transfer, pressure drop and critical heat flux in a small vertical tube with R-113, Int. J. Heat Mass Transfer 25 (1982) 945–960.

[51] M.M. Shah, A general correlation for heat transfer during subcooled boiling in pipes and annuli, ASHRAE Trans. 83 (Part 1) (1977) 205–217.

[52] M.G. Cooper, Saturation nucleate pool boiling, a simple correlation, Inst. Chem. Engng Symp. Ser. 86 (1984) 785–793.

[53] T.N. Tran, M.W. Wambsganss, D.M. France, Small circular- and rectangular-channel boiling with two refrigerants, Int. J. Multiphase Flow 22 (1996) 485–498.

[54] W. Li, Z. Wu, A general correlation for evaporative heat transfer in micro/mini-channels, Int. J. Heat Mass Transfer 53 (2010) 1778–1787.

[55] R.W. Lockhart, R.C. Martinelli, Proposed correlation of data for isothermal two-phase, two-component flow in pipes, Chem. Eng. Prog. 45 (1949) 39–48.

[56] I. Mudawar, A.H. Howard, C.O. Gersey, An analytical model for near-saturated pool boiling CHF on vertical surfaces, Int. J. Heat Mass Transfer 40 (1997) 2327–2339.

[57] I. Mudawar, R.A. Houpt, Mass and momentum transport in smooth falling liquid films laminarized at relatively high Reynolds numbers, Int. J. Heat Mass Transfer 36 (1993) 3437–3448.

[58] W. Qu, I. Mudawar, Measurement and prediction of pressure drop in two-phase micro-channel heat sinks, Int. J. Heat Mass Transfer 46 (2003) 2737–2753.

[59] W. Qu, I. Mudawar, Flow boiling heat transfer in two-phase micro-channel heat sinks-II. Annular two-phase flow model, Int. J. Heat Mass Transfer 46 (2003) 2773–2784.

[60] S.M. Kim, I. Mudawar, Theoretical model for local heat transfer coefficient for annular flow boiling in circular mini/micro-channels, Int. J. Heat Mass Transfer 73 (2014) 731–742.

[61] S.J. Kline, The purposes of uncertainty analysis, J. Fluids Eng. 107 (1985) 153–160.

[62] R.J. Moffat, Describing the uncertainties in experimental results, Exp. Therm. Fluid Sci. 1 (1988) 3–17.

[63] S.M. Kim, I. Mudawar, Theoretical model for annular flow condensation in rectangular micro-channels, Int. J. Heat Mass Transfer 55 (2012) 958–970.

[64] G.F. Hewitt, A.H. Govan, Phenomenological modelling of non-equilibrium flows with phase change, Int. J. Heat Mass Transfer 33 (1990) 229–242.

[65] P.B. Whalley, P. Hutchinson, G.F. Hewitt, The calculation of critical heat flux in forced convection boiling, in: Proc. Fifth Int. Heat Transfer Conf., Tokyo, Japan, Paper B6.11, 1974, pp. 290–294.

[66] S. Sugawara, Droplet deposition and entrainment modeling based on the three-fluid model, Nucl. Eng. Des. 122 (1990) 67–84.

[67] I. Kataoka, M. Ishiii, A. Nakayama, Entrainment and deposition rates of droplets in annular two-phase flow, Int. J. Heat Mass Transfer 43 (2000) 1573–1589.

[68] I.I. Paleev, B.S. Filippovich, Phenomena of liquid transfer in two-phase dispersed annular flow, Int. J. Heat Mass Transfer 9 (1966) 1089–1093.

[69] Y. Taitel, A.E. Dukler, A model for predicting flow regime transitions in horizontal and near horizontal gas-liquid flow, AIChE J. 22 (1976) 47–55.

[70] A.H. Govan, Modelling of Vertical Annular and Dispersed Two-Phase Flows Ph. D. thesis, University of London, Imperial College, 1990.

[71] G.B. Wallis, One Dimensional Two-Phase Flow, McGraw-Hill, New York, 1969.

[72] R.K. Shah, A.L. London, Laminar flow forced convection in ducts: A source book for compact heat exchanger analytical data (Supl 1), Academic Press, New York, 1978.

[73] W.M. Rohsenow, J.P. Hartnett, Y.I. Cho, Handbook of Heat Transfer, third ed., McGraw-Hill, New York, 1998.

[74] W.M. Kays, Heat transfer to the transpired turbulent boundary layer, Int. J. Heat Mass Transfer 15 (1972) 1023–1044.

[75] W.M. Kays, M.E. Crawford, Convective Heat and Mass Transfer, second ed., McGraw-Hill, New York, 1980.

[76] H. Ueda, R. Moller, S. Komori, T. Mizushima, Eddy diffusivity near the free surface of open channel flow, Int. J. Heat Mass Transfer 20 (1977) 1127–1136.

[77] I. Mudawar, M.A. El-Masri, Momentum and heat transfer across freely-falling turbulent liquid films, Int. J. Multiphase flow 12 (1986) 771–790.

[78] S.M. Zivi, Estimation of steady-state steam void-fraction by means of the principle of minimum entropy production, J. Heat Transfer 86 (1964) 247–252.

[79] C.L. Ong, J.R. Thome, Macro-to-microchannel transition in two-phase flow: part 1 – two-phase flow patterns and film thickness measurements, Exp. Therm. Fluid Sci. 35 (2011) 37–47.

[80] T.H. Lyu, I. Mudawar, Simultaneous measurement of thickness and temperature profile in a wavy liquid film falling freely on a heating wall, Exp. Heat Transfer 4 (1991) 217–233.

[81] C.D. Meinhart, S.T. Wereley, J.G. Santiago, PIV measurements of a microchannel flow, Exp. Fluids 27 (1999) 414–419.